Phenomenology and Kinematics of Discrete Plastic Deformation Events in Amorphous Silicon: Atomistic Simulation Using the Stillinger-Weber Potential

by

Michael J. Demkowicz

B.S., Physics (2000)
B.S., Aerospace Engineering (2000)
B.A., Plan II Honors (2000)
University of Texas at Austin

Submitted to the Department of Mechanical Engineering
in Partial Fulfillment of the Requirements for the Degree of
Master of Science in Mechanical Engineering

at the

Massachusetts Institute of Technology

February 2004

Signature of Author.....
Department of Mechanical Engineering
January 6, 2004

Certified by.....
Ali S. Argon
Professor of Mechanical Engineering
Thesis Supervisor

Accepted by.....
Ain A. Sonin
Chairman, Department Committee on Graduate Students

PHENOMENOLOGY AND KINEMATICS OF DISCRETE PLASTIC DEFORMATION EVENTS IN AMORPHOUS SILICON: ATOMISTIC SIMULATION USING THE STILLINGER-WEBER POTENTIAL

by

MICHAEL J. DEMKOWICZ

Submitted to the Department of Mechanical Engineering
on January 6, 2004 in partial fulfillment of the
requirements for the Degree of Master of Science in
Mechanical Engineering

ABSTRACT

The need to understand plastic deformation in amorphous covalently bonded materials arose from the unique mechanical properties of disordered intergranular layers in nc-TiN/a-Si_3N_4 ceramic composites. Silicon was chosen as a model disordered network solid for the purpose of conducting feasible atomistic computer simulations of plastic deformation. Amorphous silicon structures were created by melting and quenching using a molecular dynamics algorithm. These structured were plastically deformed by conjugate gradient static energy minimization. Atomic level analysis was carried out using appropriately generalized notions of stress and strain.

Plastic deformation was found to occur in a series of discrete stress relaxations, each one of which was accompanied by a well localized atomic level rearrangement. The transforming regions were roughly ellipsoidal in shape and involved the cooperative motion 100-500 atoms spanning a length scale of 0.7-2.5nm. This length scale is large in comparison to the typical thickness of disordered intergranular layers in nanocrystalline ceramic composites, indicating that the plastic relaxation process in such intergranular layers cannot be the same as the one found in bulk amorphous covalent solids.

Thesis Supervisor: Ali S. Argon

Title: Professor of Mechanical Engineering

Table of contents

1. Introduction

The motivation for undertaking an investigation of plastic deformation in amorphous silicon came from the unique mechanical properties exhibited by nc-TiN/a-Si_3N_4 nanocrystalline covalently bonded ceramic composite materials produced by S. Veprek and coworkers at the Technical University of Munich in Garching, Germany. These materials are created as thin films by either plasma or chemical vapor deposition techniques (PVD and CVD, respectively) have shown ultrahardness under microindentation on the order of 70-100GPa, i.e. commensurate with the hardness found in diamond films (Argon and Veprek [2002]). Additionally, these materials exhibit excellent microstructure stability at high temperature: they only begin to recrystallize at about 1300K.

The excellent mechanical behavior and thermal stability of these materials has made them excellent candidates for application as coatings for high-speed, high-temperature machine tools. Indeed, they hold a significant advantage over carbon-based coatings because the latter tend to dissolve easily into the substrate upon which they were deposited if said substrate is iron-based (e.g. low carbon steel). Today, nc-(AlTi)N/a-Si_3N_4 composite ceramic coatings—whose structure is similar to the nc-TiN/a-Si_3N_4 coatings that motivated this work—are commercially available through a joint venture between PLATIT AG[1] and SHM Ltd.[2].

Aside from their undeniable technological importance, nanocrystalline TiN/amorphous Si_3N_4 composite ceramic coatings pose a significant challenge to our current understanding of the processes underlying mechanical behavior of covalently bonded nanocrystalline materials. Polycrystalline metals with grain sizes on the order of micrometers exhibit the well-known Hall-Petch effect: their strength increases with decreasing grain size. Once the grain sizes reach 10-20 nanometer scales (Yip [1998]), however, this trend is reversed and further decreases in grain size are accompanied by decreases in material strength. Much like polycrystalline metals, nc-TiN/a-Si3N4 ceramic

[1] http://www.platit.com/
[2] http://www.shm-cz.cz/

composites exhibit an increase in strength with decreasing grain size. Unlike in nanocrystalline metals, however, nanocrystalline ceramic composite coatings continue to increase in strength while grain size decreases to as low as 3-5 nm in diameter (Argon and Veprek [2002]).

This stark difference between the mechanical behavior of metallic and ceramic nanocrystalline materials suggests an important question concerning the differences in mechanisms of plastic deformation in these two materials. In metallic nanocrystalline materials, the crossover from increasing to decreasing strength with decreasing grain sizes is attributed to the growing importance and eventual predominance of localized grain boundary deformation over the increasingly difficult dislocation-mediated plasticity of the crystallite grains themselves (Schiotz *et al.* [1998]). Dislocation-based plasticity of crystalline grains in ceramic nanocrystalline materials is expected to be at least as difficult as in the case of metals (because of the higher lattice resistance of covalently-bonded materials). The lack of eventual softening with decreasing grain size in ceramic composites, however, suggests that the mechanisms that enable grain boundary plasticity in nanocrystalline metals either do not operate in ceramic composites or are far more difficult to activate.

The goal of the present research is to shed light on the nature of mechanisms of plastic deformation in grain boundaries of covalently bonded nanocrystalline materials with the hope of explaining the ultrahardness of ceramic composite coatings. Studies of the distribution of the TiN and Si_3N_4 phases in nc-TiN/a-Si_3N_4 ceramic composite coatings have shown that the TiN aggregates into nanocrystallites of approximately 4-6 nm size while Si_3N_4 forms a disordered intergranular component (Argon and Veprek [2002]). The proportion of TiN and Si_3N_4 in the coatings is such as to allow the intergranular material to percolate through the system, wetting the nc-TiN grains with a layer of disordered material approximately 1-3 atomic diameters thick. Because of the difficulty of dislocation motion in the nc-TiN grains, it is this intergranular layer that is expected to govern the plastic deformation behavior of the nc-TiN/a-Si_3N_4 ceramic composite material as a whole.

The method we have chosen to address the problem described above is atomistic computer simulation using empirical potentials. Such methods have been successfully

applied in studying the mechanical behavior of nanocrystalline metals (Schiotz and Jacobsen [2003]; Yamakov *et al.* [2002]) and the structure of covalently bonded nanocrystalline materials (Keblinski *et al.* [1996a]). Unfortunately, empirical potentials for materials with complex bonding behavior are very difficult to formulate. The nc-TiN/a-Si_3N_4 coatings under investigation here belong to the category of materials with high bonding and chemical complexity. No empirical potentials have been developed that would be capable to accurately representing the interactions among its three component elements.

In light of the difficulties involved in modeling nc-TiN/a-Si_3N_4 in its full chemical complexity, an alternative approach was pursued. Instead of attempting to replicate the behavior or nc-TiN/a-Si_3N_4 specifically, an investigation was undertaken on a simpler (elemental) covalently bonded material for which many empirical potentials have been developed and tested: silicon. This approach allows us to effectively separate the influence on mechanical behavior of covalent bonding from effects that could arise from chemical (e.g. stoichiometric) constrains. As such, it simplifies the problem at hand to a manageable form while retaining the most important qualitative distinction between ceramic composites and nanocrystalline metals: the covalent vs. metallic (respectively) nature of interatomic bonding.

Finally, the intergranular material in nc-TiN/a-Si_3N_4 ceramic composites has been described as a disordered layer 1-3 atomic dimensions in thickness (Argon and Veprek [2002]). Such intergranular layers have been observed in Si both experimentally (Furukawa *et al.* [1986]) and in simulations (Keblinski *et al.* [1996b]). In investigating plastic deformation in these layers, one must distinguish between mechanical behaviors ascribable to the disordered material in its bulk form from that which results from the high degree of confinement of the material between neighboring nondeforming crystallites. Unfortunately, to date there has been little research done on the large-strain plastic deformation behavior of covalently bonded disordered materials. Therefore, as a first step to understanding plasticity in confined disordered layers of covalently bonded material, an effort was made to elucidate the plastic deformation behavior of covalently bonded materials in bulk form. This manuscript describes the results of an investigation

into the phenomenology of unit plastic deformation events in the chosen model covalently bonded bulk amorphous material: amorphous silicon (a-Si).

2. Background

This section presents a literature survey of work done in areas that serve as background and motivation for the approaches taken in the present research.

2.1 Deformation mechanisms of nanocrystalline metals

Polycrystalline metals exhibit marked dependence in shear resistance on the length scale (e.g. diameter) of their constituent grains. For grain sizes in excess of about 10-20nm, material plastic resistance is observed to increase as approximately the inverse square root of the grain size. The details of this dependence—known as the Hall-Petch relationship (Hall [1951]; Petch [1953])—remain largely unexplained to this day. Nevertheless, it is generally thought that it arises as a result of the increasing difficulty of nucleating and propagating dislocations in grains of decreasing size (Yamakov *et al.* [2002, 2001]).

At grain sizes of about 10-20nm the Hall-Petch relationship breaks down, i.e. further decreases in grain size are not accompanied by increases in material plastic resistance (Yip [1998]). The nature of plastic deformation in this transition regime is thought to be extremely complicated since in it dislocation mechanisms (which remain operative to some extent) couple strongly with grain boundary processes resulting in phenomena as diverse as nucleation of dislocations or stacking faults from grain boundary edges and formation of new grains (Yamakov *et al.* [2002]).

At grain sizes below 10-20nm, dislocation motion in the grain interiors becomes so difficult and the volume fraction of grain boundary material so high that plastic flow occurs almost exclusively by means of grain boundary shear mechanisms. Such processes have been observed in computer simulations of deformation of nanocrystalline metals with grain sizes of 3-6nm (Schiotz *et al.* [1998]). Emission of partial dislocations and stacking faults is also observed during the course of deformation, but this phenomenon was shown not to contribute strongly to the permanent accumulation of plastic strain in

the sample as a whole. By comparison, the highly localized atomic rearrangement events observed between neighboring nanocrystalline grains lead to significant stress relaxation and are therefore thought to be the most effective mechanism of plastic strain accumulation.

The term coined to describe the overall effect of the discrete stress relaxation events occurring in the intergranular regions of nanocrystalline metals—"grain boundary sliding"—gives an intuitive mesoscale description of deformation in these materials. Namely, intergranular regions are seen as layers whose inherent disorder makes them fertile sites for undergoing large strain plastic shear flow. Connections have also been proposed between the deformation processes in disordered grain boundaries and those observed in glassy metals due to similarities in the structure of local atomic environments in these two settings (Wolf *et al.* [1995]; Lund and Schuh [2003]). More fundamental insight into the mechanisms that enable "grain boundary sliding" is nonetheless lacking.

2.2 Grain boundary structure in nanocrystalline network solids

The argument for the increasing difficulty of dislocation motion with decreasing grain sizes in metals holds all the more true for covalently bonded materials such as the nc-TiN/a-Si_3N_4 ceramic composites or nc-Si. The reason for this conclusion is that the lattice resistance to dislocation motion is vastly higher in covalently bonded materials than in metals. FCC metals typically have a negligible lattice resistance (about 20 MPa (Olmsted *at el.* [2001])) and BCC metals have lattice resistances in the range of 600-900 MPa (Conrad [1963]) while the lattice resistance in Si is around 13 GPa (Ren *et al.* [1995]), i.e. almost a full three orders of magnitude higher. In Cu, dislocation motion ceases to play an important role in plastic flow behavior at grain sizes on the order of 10-20nm. Thus, in nc-TiN/a-Si_3N_4, where the size of crystalline grains is thought to be in the range of 4-6nm, the contribution of dislocation-mediated plasticity to the overall plastic response of the material can be safely ignored. As a result, the structure and mechanical behavior of intergranular material in nanocrystalline covalently bonded materials is of prime importance to understanding the plastic flow behavior of such materials.

While there have been no investigations of the mechanisms of plastic deformation by computer simulation in the case of nanocrystalline covalently bonded materials such as nc-Si, a number of studies of grain boundary structure have been undertaken (Keblinski *et al.* [1996a, 1996b]). These investigations have shown that for high angle boundaries between neighboring grains (i.e. for orientations that are not among the few special orientations with extremely low interface energies) there forms a disordered intergranular layer of 1-3 atomic dimensions in thickness. Using computer simulations of intergranular structure in silicon bicrystals, Keblinski *et al.* [1996b] have demonstrated on a number of crystal orientations that structurally indistinguishable disordered layers form both when an initially unrelaxed grain boundary is annealed as well as when two neighboring crystal slabs are allowed to grow out from the melt until they impinge upon each other. Furthermore, they show that the disordered intergranular structure is thermodynamically stable in the sense that its overall energy is smaller than that of the corresponding unrelaxed grain boundaries.

Keblinski *et al.* [1996a] have also carried out computer simulations to study the structure of grain boundaries in nanocrystalline silicon. Starting with a configuration of grains that avoided all high symmetry grain boundaries, they annealed the sample and found that—much as in the case of the bicrystal—there formed a disordered intergranular layer of 1-3 atomic diameters thickness. Structurally indistinguishable grain boundaries formed when the same configuration of crystalline grains was grown from the melt, starting with a set of properly oriented crystalline seeds. Radial and angular distribution functions constructed at grain boundaries, triple junctions, and 4- and 6-fold points demonstrated that intergranular material in each of these regions could be considered disordered.

Experimental evidence in support of the existence of disordered intergranular material between highly misoriented crystalline slabs has also been found. When developing the technology of joining perfectly crystalline silicon wafers for semiconductor purposes, Furukawa *et al.* [1986] observed that the nature of the bond between wafers depended sensitively on the crystalline misorientation of the silicon wafers. In particular, when the surfaces being joined had little or no misorentation, a nearly perfect crystalline structure was formed. When two (100) surfaces were

misoriented by 45 degrees, a thin grain boundary whose structure was difficult to discern resulted. If (100) and (111) surfaces misoriented by 45 degrees were joined, however, the resulting annealed intergranular structure was a disordered layer of thickness around 10 atomic diameters.

Careful study of the structure and distribution of components in the nc-TiN/a-Si_3N_4 ceramic composites suggests that the TiN phase forms crystalline grains 4-6nm in size while Si_3N_4 forms a 1-3 atomic diameter-thick disordered layer that wets the nc-TiN grains. This conclusion was reached after studies of stoichiometry (Veprek and Argon [2002]) revealed that the proportions of TiN to Si_3N_4 were just right to allow such wetting to take place. Therefore, the expected intergranular structure of Si_3N_4 in nc-TiN/a-Si_3N_4 coincides with the structure of intergranular layers in nc-Si as simulated by Keblinski *et al.* [1996a], lending support to the choice of investigating the mechanical behavior of the chemically complex nc-TiN/a-Si_3N_4 using elemental silicon as a model system.

2.3 Deformation mechanisms in glassy metals and polymers

As was explained in the preceding sections, plastic deformation in nanocrystalline covalently bonded materials is expected to take place chiefly in the intergranular regions. These regions—as indicated by simulation and experiment—can be described as layers of disordered material confined by neighboring (nondeforming) crystallites. In order to understand the nature of deformation in these intergranular layers, however, it is necessary to distinguish between deformation characteristics ascribable to plastic deformation in bulk disordered covalently bonded materials from those that can be attributed to the severe degree of confinement to which these materials are exposed within the context of nanocrystalline structure. To obtain this distinction, plastic deformation in bulk disordered network materials must first be understood. Unfortunately, to date there have been few investigations of plastic deformation in such materials. To gain some background on deformation in other types of amorphous solids, therefore, we review deformation processes in glassy metals and polymers.

Before computing capabilities became sufficiently great to allow for meaningful atomistic simulations of plastic deformation, other methods of modeling the collective behavior of systems composed of discrete particles interacting with spherical potentials were developed. Among the most notable is the bubble raft technique, which allowed for the investigation of systems composed of hundreds of constituent particles in two dimensions. As a means to visualizing complex rearrangements occurring under deformations applied externally, this method was an invaluable tool in the qualitative study of atomic scale behavior of disordered materials (Argon and Kuo [1979]). Upon complete description of the interbubble potential function the method became quantitative as well and yielded some of the earliest insights into the mechanisms of plastic deformation in disordered materials whose constituent atoms could be thought of as interacting with pair potentials, namely metallic glasses (Argon and Shi [1983]). Because of its value as a rapid visualization tool, the bubble raft technique is still used today (Van Vliet and Suresh [2002]).

Using the bubble raft method, Argon and Shi [1983] constructed a two dimensional representation of a metallic glass by mixing bubbles of two different sizes and not allowing them to arrange into crystalline domains. They then deformed the bubble raft by externally applying displacements to the walls of the raft in a way that could be interpreted as applying total system-wide strain increments. In the course of the deformation process, they observed that certain regions of the bubble raft suddenly underwent large, localized bursts of displacement. These localized rearrangements usually involved about 10 atoms. Analysis of changes in bubble positions within the active regions before and after a rearrangement clearly indicated that these transformations were shearing events and led to the irreversible accumulation of shear strain, i.e. to localized plastic deformation. Using the interbubble potential developed earlier, Argon and Shi were able to use their insight into the kinematics of atom cluster rearrangements to calculate a distribution of activation energies associated with the transformations.

These findings stood in stark contrast to the Eyring hypothesis of flow in liquids (Eyring [1936]) that—until then—had been considered a likely candidate (on grounds of structural similarity (Kauzmann [1948])) for explaining flow in glassy materials. This

hypothesis stipulated that individual atoms of a liquid or glass could irreversibly change their position in a manner similar to diffusion when an opening appeared in the surrounding medium. As indicated, however, bubble raft visualizations indicated a mechanism involving the collective motion of around 10 atoms, not just 1 as Eyring had proposed. Even more seriously, the motion of a single atom moving through open channels in the surrounding medium is a mechanism that is inherently incapable of producing shear transformations since shear cannot even be meaningfully defined unless at least 4 interacting, neighboring atoms rearrange in a cooperative manner.

In a later series of molecular dynamics computer simulations on a two dimensional single component system of particles interacting with a central potential, Deng *et al.* [1989] verified the results found in the bubble raft studies. Defining a local strain measure, they were able to identify transforming regions as those in which high levels of deviatoric strain had suddenly been created. Furthermore, they addressed the question of the correlation of excess volume distribution to the localization of shear transformations (Turnbull and Cohen [1961, 1958]; Cohen and Turnbull [1959]). By using a local structure descriptor based on the Voronoi tessellation around atomic positions, Deng verified that certain regions within the model metallic glass were more prone to undergoing irreversible transformation than others.

Building upon the work of Deng, Bulatov and Argon [1994] constructed a simplified model of metallic glasses that presupposed a single plastic deformation mechanism that could be activated by both thermal motion and mechanical stresses. This assumption was meant to combine the observations that plastic deformation in glassy metals is local and occurs preferentially at certain sites. Through a series of simulations, Bulatov showed that this single deformation mechanism—because of elastic interactions between transforming regions and the surrounding nondeforming matrix—is able to reproduce all the high and low temperature behaviors observed in metallic glasses.

The work of Bulatov and Argon [1994] makes no reference to the type of interatomic potential governing the system from which the constitutive parameters that enter into his model (the form of thermal and mechanical activation behavior) are taken. His general conclusions are therefore expected to apply to disordered covalently bonded materials as much as to metallic glasses. It is nevertheless instructive to step back and

observe how differing empirical atomic interactions *do* influence the plastic deformation behavior of disordered media by reviewing computer simulations of such behavior in glassy polymers.

Unlike metals, polymers are governed by two types of atomic interaction: strong covalent bonds along polymer chain backbones and weak van der Waals-type interactions between atoms on separate polymer chains (Theodorou and Suter [1985]). This comparatively more complex form of bonding along with a variety of possible chain conformations and branchings leads to a large variety of possible local structure features in polymers (Theodorou and Suter [1986]; Hutnik *et al.* [1991]). The kinematics of plastic transformation in these materials is similarly more convoluted: they involve significantly larger numbers of participating atoms than in metallic glasses (on the order of hundreds (Mott *et al.* [1993])) as well as a large variety of discernable structural rearrangements (Hutnik *et al.* [1991]).

Nonetheless, despite the intricacies of bonding and transformation kinematics apparent in polymers, certain features of the fundamental mechanisms of plasticity in these materials are entirely analogous to those occurring in the far simpler metallic glasses. Deformation in polymers also occurs in discrete, localized bursts. It can be activated thermally as well as mechanically and the atomic rearrangements that accompany plastic deformation can be characterized as shear transformations (Mott *et al.* [1993]). Finally, the relaxation strain spectra found in computer simulations—according to Bulatov—are not inconsistent with operation of a finite number of activated processes.

2.4 Why dislocations do not mediate plasticity in amorphous solids

The success of dislocation mechanics in explaining crystal plasticity prompted some investigators (Gilman [1968]) to suggest that the notion of "dislocation" can be sufficiently generalized so that a dislocation-based structure analysis could be performed on disordered materials. The difficulty with constructing such a generalization lies in the inherent reference to the crystal lattice in the traditional definition of edge and screw dislocations: both are characterized by their respective Burgers vectors (McClintock and

Argon [1966]). Such a characterization is impossible in materials that by definition do not contain a crystalline component. A number of generalizations were nevertheless made (Gilman [1968]), but only one resulted in a distinguishing criterion sufficiently unambiguous to be applied in the context of atomistic simulation. This criterion made no reference to the underlying core configuration of "generalized dislocations" and focused instead on the effect that a dislocation produces in the surrounding material. Namely, it claimed that a generalized dislocation is the kind of structure difference between two configurations that produces a difference in stress fields between these two configurations that can be characterized by the well-known stress fields produced in a crystal lattice by the introduction of screw and edge dislocations (Chaudhari [1979]).

Using this definition as a starting point, Chaudhari *et al.* conducted computer simulations to investigate whether it would be possible to observe generalized dislocations in a metallic glass. They started by creating large samples of disordered material and characterizing the stress distributions within them. They then followed a procedure borrowed from elementary mechanics of materials textbooks for introducing dislocations into these samples: the removal of a half-plane of atoms to create an edge and the shear-like shifting of a half-plane of atoms to create a screw (McClintock and Argon [1966]). Analysis of the resulting stress fields revealed that the difference in the distribution of stresses between the new and initial sample configurations were indeed in good agreement with those observed in crystal lattices.

Upon equilibration by potential energy minimization of the new configurations, however, the stress field associated with the edge dislocation construction vanished: no coherent difference between the initial and equilibrated edge configuration could be found. In the case of the screw construction, equilibration did not destroy the characteristic stress fields of screw dislocations in crystal lattices. Neverthelesss, the elastic energy stored in the stress fields associated with this construction was so high compared to the typical activation energy of localized shearing transformations of the kind investigated by Argon and Shi [1983] as well as Deng *et al.* [1989] that under normal loading conditions these shearing transformations would quickly dissipate the generalized screw dislocation. Experimental studies of dissipation of dislocation

structures in crystals under irradiation confirm the relative instability of highly stressed regions in amorphous media (Cherns *et al.* [1980]).

The conclusion that can therefore be drawn from the work of Chaudhari *et al.* is that generalized edge dislocations are not stable within a disordered medium. Generalized screw dislocations, on the other hand, though stable and therefore conceivably observable, cannot be responsible for plastic flow in disordered materials because their operation is not energetically favorable compared to other deformation mechanisms (localized shear transformations) known to operate in these same materials (Argon [1981]).

2.5 Structure and rigidity of covalent network materials

As was pointed out in the previous section, metallic systems can be seen as interacting with simple spherical potentials while polymers involve strong covalent bonding along backbones and weak bonding between individual chains. Purely covalently bonded materials—also known as covalent network materials—involve only strong atomic interactions of the kind found along polymer backbones. Thus, such materials represent a state of local atomic constraint more extreme than that found in either metals or polymers. For this reason, network materials could be expected to exhibit some particularities in the character of unit shear transformations occurring within them during plastic deformation much along the lines of the differences found between unit shearing events in glassy metals and polymers.

Although no earlier work has been done on elucidating the details of unit plastic transformations in disordered covalently bonded solids, there have been investigations into how the bonding structure of such materials affects their rigidity. A simple local constraint model may be used to elucidate the effect of the average number of covalent bonds between neighboring atoms on the rigidity of a random network material (Thorpe et al. [2000]). This approach—first proposed as a means to finding compositions for optimal glass formability in chalcogenides (Phillips [1979, 1981a, 1981b])— predicts a

linear dependence of the concentration f of zero frequency eigenmodes on the average coordination:

$$f = 2 - \tfrac{5}{6}\langle r \rangle$$

In particular, according to this treatment there are no more such modes above an average coordination of 2.4. Therefore, above this critical value the potential energy of a well-relaxed covalently bonded system is likely to be "stiff" in all eigendirections. These predictions have been verified by simulations performed on random bond network models (Thorpe et al. [2000]) and fall into a general class of problems often referred to as "rigidity percolation" (Kantor [1984]).

Materials with average coordination higher than 2.4 can be considered covalent network materials. The amorphous Si_3N_4 intercrystalline layers in nc-TiN/a-Si_3N_4 materials that motivated this research have an average coordination of 3.5>2.4, i.e. they can be thought of as covalent network materials. Silicon—whose average coordination is usually not below 4—results in a level of local atomic constraint that also classifies it as a covalent network material.

The best-known model of the structure of well relaxed four-fold coordinated random network materials was proposed by Zachariasen [1932]. This view holds that covalent bonds between atoms are so stiff that any change in their equilibrium length would incur a heavy energy penalty. Thus, energy would be minimized in a disordered covalently bonded material if lack of long-range order were accommodated through structural features other than changes in bond lengths, in particular through bond angle distortions (Zallen [1979]). This structural model is called the continuous random network (CRN). Its radial distribution function is clearly distinguishable from that of disordered materials interacting through spherical potentials as the latter gives evidence of significant variability in bond lengths as well as of ill-defined second nearest neighbor positions (Zallen [1979]).

3. Methods

This section describes the computational methods used to model the structure and deformation behavior of amorphous silicon. It also describes analysis methods used to extract useful information from the computer simulations.

3.1 Empirical potentials

By the Born-Oppenheimer approximation (Ziman [1995]), under temperatures and pressures characteristic of our everyday experience the ground state energy of a group of atoms can be found by assuming that electronic degrees of freedom relax completely while nuclear positions remain unchanged. Forces acting on individual nuclei are then described by the variation in this ground state energy with nuclear positions. In principle, one could accurately simulate the dynamics of an arbitrarily large collection of atoms using this semi-quantum mechanical approach. In practice, however, such an *ab initio* scheme of atomistic simulation is severely limited by the inadequate capabilities of modern computers and can only be applied to short-time simulations of groups of about 100 atoms without resorting to use of large parallel machines. Since the research described here requires several thousand atoms and long annealing periods, the high accuracy of *ab initio* must be traded for the high efficiency of simulation based on empirical potentials.

Atomistic simulation based on empirical potentials incurs significantly fewer computational costs than that based on *ab initio* methods because instead of relaxing electronic degrees of freedom in order to determine the ground state energy of a given configuration of atomic nuclei, the form of the ground state energy is assumed *a priori*. The forces on individual nuclei are then simply determined as the negative gradient of the system-wide potential energy (the assumed ground state energy) with respect to the positions of said atomic nuclei.

In most cases the form of the assumed potential is a sum of terms arising from interactions of pairs, triples, quadruplets, etc. of atoms:

$$V(r_1, r_2, ...r_N) = \sum_{i<j} V_2(r_i, r_j) + \sum_{i<j<k} V_3(r_i, r_j, r_k) + ... \qquad 3.1$$

Generic physical insights are used to choose a functional form for the potential energies V_2, V_3, etc. These functional forms generally include undetermined parameters that can be chosen to make the behavior of a collection of atoms governed by the empirical potential conform as closely as possible to the behavior of the substance being modeled. Naturally, all functional forms entering into the empirical potential must satisfy the requirements of objectivity and frame indifference.

A simple empirical potential often used in examples is the classic Lennard-Jones potential (Allen and Tildesley [2000]):

$$V = 4\varepsilon \sum_{j<i} \left(\left(\frac{\sigma}{r_{ij}} \right)^{12} - \left(\frac{\sigma}{r_{ij}} \right)^{6} \right)$$

where ε and σ are the characteristic energy and length, respectively, and r_{ij} is the distance between atoms i and j. This potential consists entirely of pair interaction (i.e. two-body) terms and contains two undetermined parameters. It was originally meant to describe noble gasses, but potentials of similar form have been used to simulate metallic glasses as well (Deng [1989]). The functional form of the two-body term is shown in figure 3.1 and the motivation behind it is easy to understand. If the distance between a pair of atoms increases indefinitely we assume that the forces on both atoms will approach zero, i.e. the slope of the potential energy will vanish. On the other hand, if two atoms are moved sufficiently close together we know that degeneracy pressure arising from the Pauli exclusion principle (Huang [1987]; Ziman [1995]) as applied to the core electrons of the atom pair will cause the potential energy of the system to rise dramatically. Finally, we realize that atom pairs can attain a stable equilibrium distance. At this distance, the potential energy of the pair is minimized.

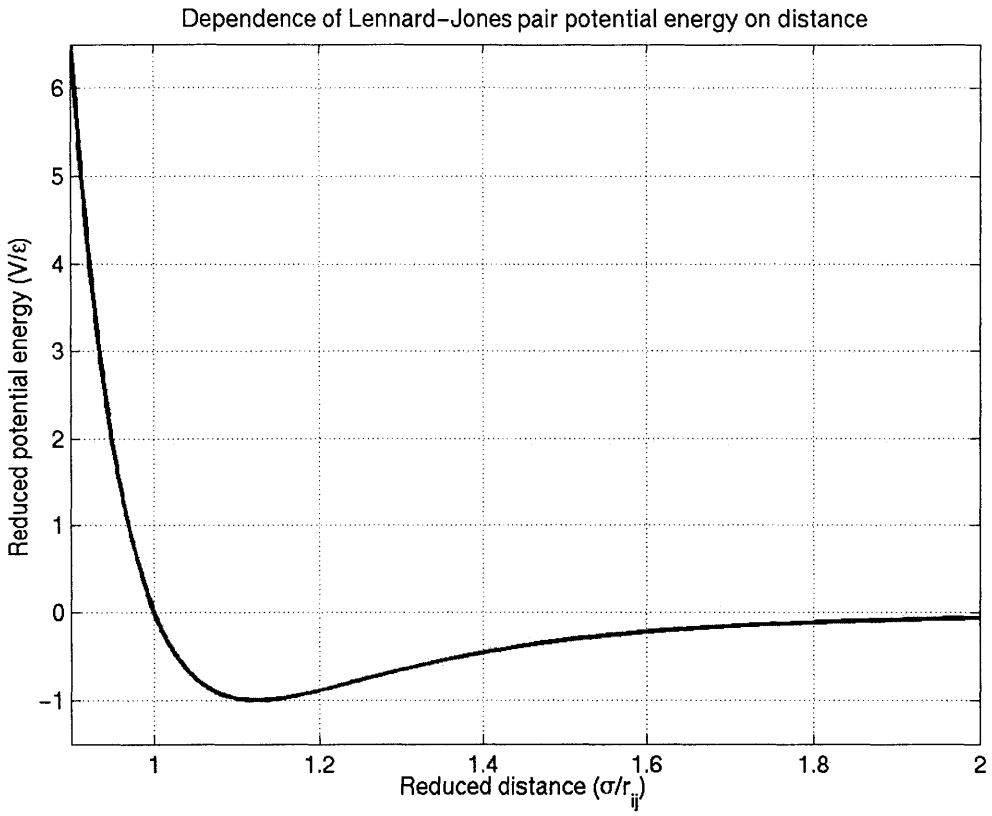

Figure 3.1: The essential physical features of the Lennard-Jones pair potential are the strong repulsion at close distances, vanishing interaction at large distances, and the intermediate equilibrium (minimum energy) state.

The lowest energy crystal configuration attainable in most spherically symmetric empirical potentials such as Lennard-Jones is the densely packed face centered cubic structure. The lowest energy STP configuration of silicon, however, is diamond cubic. Therefore, to create a basic empirical potential for silicon one must incorporate at least one physical insight in addition to those described above, namely that potential interactions favoring the arrangement of bonds between neighboring atoms at the tetrahedral angle of $\theta = \cos^{-1}\left(-\frac{1}{3}\right) \approx 109.5°$ be added. The distinguishing features of empirical potentials created to model silicon center around the way in which this physical insight was incorporated into the functional form of the potential and in the number of additional modifications made so that the behavior of an atomic system modeled by the

potential in question accorded with subtler experimentally determined characteristics of silicon.

En excellent review of available empirical potentials for silicon was given by Balamane *et al.* [1992]. Here, however, we shall only describe the most commonly used ones, namely those due to Stillinger and Weber [1985], to Tersoff [1986], and the EDIP (Bazant *et al.* [1997]). Of these three, the Stillinger-Weber potential was chosen for the present work due to its simplicity and good semi-quantitative agreement with the behavior of real silicon. For this reason, it shall be described in greater detail than the other two empirical potentials.

The Stillinger-Weber potential consists of a summation of two- and three-body potential interaction terms:

$$V(r_1, r_2, ...r_N) = \sum_{i<j} V_2(r_{ij}) + \sum_{i<j<k} V_3(r_{ij}, r_{jk}, r_{ik})$$

where r_{ij} indicates the distance between atoms i and j. The potential contains characteristic length and energy parameters σ and ε. These parameters are used to nondimensionalize the component terms V_2 and V_3 as follows:

$$V_2(r_{ij}) = \varepsilon f_2(r_{ij}/\sigma)$$
$$V_3(r_{ij}, r_{jk}, r_{ik}) = \varepsilon f_3(r_{ij}/\sigma, r_{jk}/\sigma, r_{ik}/\sigma)$$

The functional form of the two-body terms f_2 was chosen to be

$$f_2(r) = \begin{cases} A(Br^{-p} - r^{-q})e^{\frac{1}{r-a}}, r < a \\ 0, r > a \end{cases}$$

This functional form embodies the same physical intuitions as does the Lennard-Jones potential. The exponential term applies a "potential cutoff radius," i.e. it is a construction that ensures that the value of the two-body interaction and all of its derivatives goes to

zero at the distance specified by parameter a. A, B, p, q also denote parameters and can be chosen to fit the form of the potential to experimental results for silicon.

The three-body potential terms have the form

$$f_3(r_{ij}, r_{jk}, r_{ik}) = h(r_{ij}, r_{ik}, \theta_{jik}) + h(r_{ij}, r_{jk}, \theta_{ijk}) + h(r_{jk}, r_{ik}, \theta_{ikj})$$

$$h(r_{ij}, r_{ik}, \theta_{jik}) = \begin{cases} \lambda\left(\cos\theta_{jik} + \frac{1}{3}\right)^2 e^{\left(\frac{\gamma}{r_{ij}-a} + \frac{\gamma}{r_{ik}-a}\right)}, (r_{ij} < a) \wedge (r_{ik} < a) \\ 0, (r_{ij} \geq a) \vee (r_{ik} \geq a) \end{cases}$$

$$\theta_{jik} = \frac{r_{ij}^2 + r_{ik}^2 - r_{jk}^2}{2 r_{ij} r_{ik}}$$

The essential feature of this functional form is the $\left(\cos\theta_{jik} + \frac{1}{3}\right)^2$ term. When the bond angle θ_{jik} is precisely the tetrahedral angle found in the diamond cubic lattice configuration, the value of this term vanishes. Otherwise, it has some positive value. Therefore, the three-body interactions so constructed fulfill the requirement of favoring the four-fold coordinated configuration exhibited by silicon in its diamond cubic form. Note that the exponential term fulfills the same purpose here as in the case of two-body interactions, namely it enforces a potential cutoff radius. λ and γ are parameters of the potential.

The parameters appearing in the functional forms described above were chosen to ensure the best agreement with the experimentally observed behavior of silicon. The criteria guiding the selection were:

- Stability of the diamond cubic lattice structure at STP
- Temperature of the melting point
- Silicon contracts upon melting and forms a highly coordinated liquid form
- Lattice spacing and atomization energy of crystalline silicon

These criteria led to the following choice of parameters:

$$A = 7.049556277$$
$$B = 0.6022245584$$
$$p = 4$$
$$q = 0$$
$$a = 1.80$$
$$\lambda = 21.0$$
$$\gamma = 1.20$$
$$\sigma = 0.20951nm$$
$$\varepsilon = 50kcal/mol \approx 3.4728 \cdot 10^{-19} J$$

The behavior of the resulting empirical potential is in good semi-quantitative agreement with experiments (Luedtke and Landman [1989]), particularly for the liquid state. Its greatest drawback is its tendency to overpredict the coordination of well-relaxed amorphous silicon by about 4%. Nevertheless, its simplicity and intuitive functional form made it the most attractive model for the purposes of this study.

Unlike the Stillinger-Weber potential, the Tersoff potential includes only two-body terms:

$$V = \tfrac{1}{2} \sum_{i,j \neq i} f_c(r_{ij}) \left[A e^{-\lambda_1 r_{ij}} - B_{ij} e^{-\lambda_2 r_{ij}} \right]$$

This choice of functional form is motivated by the realization that binding-energy curves for solid cohesion and chemisorption can be described by a single dimensionless curve and three scaling parameters (Rose *et al.* [1983]) and that this behavior can be achieved by the assumption of an interatomic potential of the above form (Abell [1985]). The first exponential term in brackets describes repulsion while the second describes bonding. In order to ensure that silicon have the required tendency to form the four-fold coordinated diamond cubic structures, the value of B_{ij} could not be taken as constant. Instead, it was given a complex functional form that reflected the weakening of bond strengths in a highly coordinated atomic environment. f_c is a potential cutoff radius function.

The parameters in the final functional forms specified by Tersoff were fitted to give maximum agreement for the lattice constant, bulk modulus of bulk Si, and for the

cohesive energies of the Si_2 dimer, the diamond cubic structure, and of hypothetical Si simple cubic and FCC structures. The behavior of the potential so parametrized was tested by comparing it to results from a number of *ab inito* simulations, mainly of lattice defect structures (Tersoff [1986]). This potential was not chosen for the present study because its relatively complex functional form does not lend itself to easy algebraic manipulation nor to immediate intuitive understanding.

The EDIP (Environmentally Dependent Interatomic Potential) combines the approaches used in the Stillinger-Weber and Tersoff potentials: it includes two- and three-body interactions, both of which depend on the form of the environment of individual atoms. The highly involved parametrization of this potential (Bazant *et al.* [1997]) results in good transferability to certain types of silicon lattice defect structures (Justo *et al.* [1998]). EDIP is also capable of modeling well-equilibrated amorphous silicon structure better than Stillinger-Weber can. Nevertheless, it does not do well in reproducing certain properties of silicon in its liquid form (Keblinski *et al.* [2002]). In particular it severely underpredicts the coordination and volume contraction of the melt. Its ability to accurately model quickly quenched (suboptimally relaxed) disordered structures is therefore in question. These drawbacks together with the high complexity of EDIP made its use unattractive for the purposes of this study.

3.2 Molecular dynamics (MD) simulation

The collective behaviors of systems composed of many atoms and governed by complex interaction potentials are most commonly investigated by Monte Carlo (MC) and molecular dynamics (MD) simulations (Allen and Tildesley [2000]). The former are especially convenient in studies of long-time thermodynamic behavior, particularly if the salient unit processes are already well understood. The latter are more useful when detailed investigations of atomic level motion are called for. Therefore, in cases when little is known about the physical processes governing long time collective behavior—as in the formation of amorphous silicon from the melt and the deformation behavior of the resulting material—molecular dynamics is preferred despite the greater computational

resources it requires. The fundamentals of this simulation technique are described in this section.

Given an interaction potential, a molecular dynamics can be carried out by specifying an initial atomic configuration (including boundary conditions) and integrating the Newtonian equations of motion

$$\begin{aligned} \dot{r}_i &= p_i / m_i \\ \dot{p}_i &= -\nabla_{r_i} V = f_i \end{aligned} \qquad 3.2$$

Here r, p, m, and f denote position, momentum, mass, and force (respectively), V is the assumed interatomic potential, and i indicates one of the 3N degrees of freedom of the system (each associated with a component of a single atom's position). Equations 3.2 are integrated using a finite difference scheme such as the commonly used Gear predictor-corrector (Allen and Tildesley [2000]). In this method, time derivatives of atomic positions up to the fifth order are stored in memory. They are used to predict the future positions and their time derivatives after a suitably chosen time increment Δt. These predicted quantities are then corrected to account for information obtained from computing atomic accelerations using the interatomic potential. The computation of potential-related quantities like atomic accelerations is by far the most time-consuming step in an MD simulation. Thus, since they only require a single acceleration computation per time step, numerical integration techniques such as the Gear predictor-corrector are preferable to Runge-Kutta-type schemes in MD simulations.

Given a judicious choice of simulation parameters (such as the integration time step Δt) a simulation of the type described above results in an energy-conserving system trajectory, as predicted by equations 3.2. Additionally, a variety of specialized techniques exist to conduct simulations at constant temperature, pressure, enthalpy, Gibbs free energy, etc. (Allen and Tildesley [2000]). Many of these techniques require a modification of the equations of motion according to Gauss' principle of least constraint (Evans and Morriss [1984]). A well known example is the Hoover [1983] constant temperature algorithm which requires that instead of solving the classical Newtonian equations of motion 3.2 the MD algorithm be used to integrate

$$\dot{r}_i = p_i / m_i$$
$$\dot{p}_i = f_i - \xi\left(\left\{r_j, p_j : j = 1...3N\right\}\right) p_i$$
$$\xi\left(\left\{r_j, p_j : j = 1...3N\right\}\right) = \frac{\sum_{j=1}^{3N} p_j f_j}{\sum_{j=1}^{3N} \left|p_j\right|^2}$$

This altered set of equations of motion can be shown to generate trajectories that sample the canonical ensemble (Evans and Morriss [1983]) just as the trajectories of 3.2 sample the microcanonical.

As was mentioned before, the most time-consuming step of an MD simulation is the evaluation of an interatomic potential-related quantity such as the system potential energy or atomic accelerations. The root cause of this limitation is the need to loop over all pairs of atoms in the case of a two-body potential or all triplets of atoms in the case of a three-body one. The number of computations required therefore scales as the second and third power of the total number of atoms (respectively) and can easily exceed one billion computations per evaluation for systems containing thousands of particles. The evaluation process can, however, be made significantly faster if the form of the interatomic potential incorporates a cutoff radius, as does the Stillinger-Weber potential. In that case each atom only interacts with other atoms within a certain a distance of it. It can therefore be arranged through the use of linked-cell and Verlet neighbor lists (Allen and Tildesley [2000]) that the number of computations required scale linearly with the number of atoms, making large-scale MD simulation feasible.

3.3 Conjugate gradient static energy minimization (CGSEM) simulation

While MD is a useful method for investigating the behavior of collections of atoms obeying full Newtonian or Gauss-constrained dynamics, there are circumstances when motions of individual atoms do not have much effect on the physical phenomenon of interest and may even obscure it. Such a situation arises in the investigation of plastic

deformation mechanisms at low temperature, i.e. when diffusion does not play a major role (Argon [1996]). It is then convenient to remove atomic motion entirely and to simulate the deformation behavior of an atomic system by applying increments of the loading parameter and ensuring that the potential energy of the system is at a local minimum for each value of the externally applied load. The resulting system behavior can then be viewed as corresponding to the temperature-dependent mechanical behavior extrapolated to zero temperature, where all phenomena uniquely associated with the approach to (the physically unattainable) absolute zero have been ignored.

A simulation of the type described is often referred to as static energy minimization (SEM) simulation (Mott *et al.* [1993]) or a potential landscape method (Stillinger and Weber [1983]). Since it is generally used on systems that are thermodynamically metastable (e.g. as amorphous silicon is with respect to crystalline silicon), it does not require the attainment of global potential energy minima. An initially disequilibrated structure must simply be brought to an equilibrium configuration by minimization of potential energy to a local minimum. The core algorithm that lies at the heart of a typical SEM simulation is therefore one of the classical local minimization schemes, such as the Newton-Raphson, quasi-Newton, conjugate gradient, or steepest descent method (Bertsekas [1999]).

Newton-Raphson and quasi-Newton techniques guarantee the fastest convergence to equilibrium in the vicinity of a local minimum. Nevertheless, they require the largest computational resources and suffer from a number of inadequacies if minimization is attempted for a configuration initially far from stable equilibrium. Steepest descent is the simplest and most robust of the four schemes mentioned above, but it offers the slowest rate of convergence. The conjugate gradient (CG) method was therefore chosen for the current investigation. It offers superlinear convergence in the vicinity of a minimum, requires comparatively small computational resources per simulation step, and operates reliably for all initial configurations (Bertsekas [1999]).

The CG method—as all techniques for minimization of nonlinear functions—is an iterative method. Given a starting configuration, it produces a new one with a lower value of the function to be minimized. This cycle is then repeated using the configuration just obtained as the new starting configuration. Assume that at the beginning of the k^{th} cycle

the system is in some configuration x^k where x is a 3N-dimensional vector containing all the atomic positions. We then vary the system configuration by displacing atoms linearly along a given direction d^k (d is a 3N-D vector) by some amount α^k (α is a scalar). The displaced configuration is

$$x^{k+1} = x^k + \alpha^k d^k \qquad 3.3$$

Given some direction d^k, α can be chosen by conducting a one-variable unconstrained minimization of the potential energy $V(x^{k+1}) = V(x^k + \alpha^k d^k) = V(\alpha)$ along d^k using a line-minimization scheme such as the Brent method (Brent [1973]) or cubic interpolation (Bertsekas [1999]). Once a minimizing α is found, this procedure is repeated starting from x^{k+1} and along a new direction d^{k+1} until some previously specified convergence criterion is met.

The heart of the conjugate gradient method lies in the selection of the line-minimization direction d. The most common choice—and the one used in the current research—is due to Polak and Ribiere [1969] and can be stated briefly as

$$\begin{aligned} d^k &= -g^k + \beta^k d^{k-1} \\ \beta^k &= \frac{g^k \cdot (g^k - g^{k-1})}{g^{k-1} \cdot g^{k-1}} \\ g^k &= \nabla_x V(x^k) \end{aligned} \qquad 3.4$$

g^k—as the last line indicates—is the gradient of the potential function at configuration x^k with respect to the atomic positions x.

If in the above formula we had $\beta = 0$, the algorithm would reduce to the steepest descent method, i.e. for any initial configuration the line minimization 3.3 would be carried out in the direction where $V(x)$ decreases the fastest. Though such an approach appears reasonable at first glance, it can be shown to offer slow (often nearly linear) convergence if the minimum lies in a narrow "potential valley" (fig. 3.2). The value of selecting β as indicated in 3.4 is that every new minimization direction d^k is linearly

independent of the (k-1) previous directions. The frequent retracing along previous minimization directions apparent in the "zigzag" approach to the minimum characteristic of the steepest descent method (fig. 3.2) is therefore avoided. As a result, the conjugate gradient method yields superlinear convergence rates, sometimes even approaching the quadratic convergence of the more complex and computation-intensive quasi-Newton methods (Bertsekas [1999]).

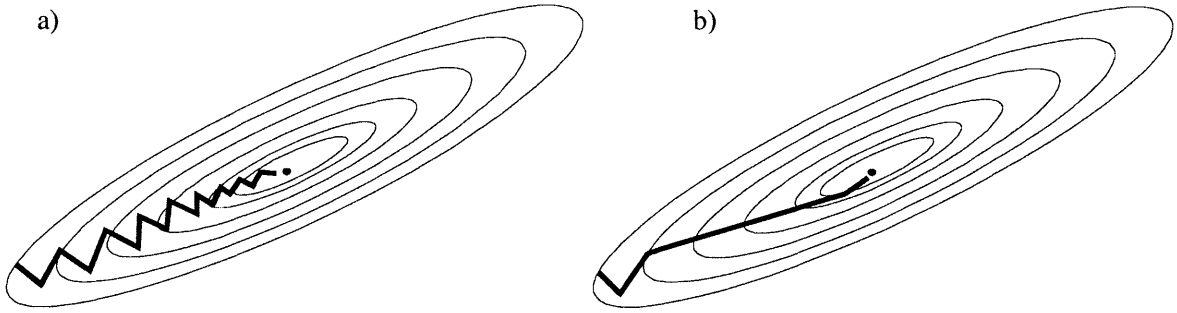

Figure 3.2: Minimization in a narrow valley. a) The steepest descent method retraces its steps in a characteristic "zigzag" pattern. b) Successive conjugate gradient directions are chosen to be linearly independent from the previous ones, leading to faster convergence.

3.4 Analysis

MD and CGSEM are capable simulating the dynamic and static structure evolution of collections of atoms, but say nothing of the task of interpreting and analyzing the output structures. Appropriate techniques must therefore be chosen and brought to bear on the results of any atomistic simulation in order to extract some physical insight from it. This section describes methods that allow the outputs of a MD or CGSEM simulation to be understood in terms of concepts commonly used in continuum mechanics, namely "stress" and "strain."

3.4.1 Atomic stress

The stress components of a system described by a potential function $V(r_1, r_2, ...r_N)$ can be expressed as (Allen and Tildesley [2000])

$$\sigma_{\alpha\beta} = k_B T \rho \delta_{\alpha\beta} + \frac{1}{\mathcal{V}} \frac{\partial V}{\partial u_{\alpha\beta}} \qquad 3.4$$

The first term on the right hand side arises from thermal motion and depends linearly on temperature and density (k_B is the Boltzmann constant). The second term is the variation of the potential energy with the appropriate component of the deformation gradient u. $\mathcal{V}$ is the total system volume.

The derivation of expression 3.4 interprets "stress component" as the appropriate resolved force component per unit area acting across any chosen surface and follows the approach typically used in the kinetic theory of gasses (Haile [1997]). For the purposes of atomic-level structure analysis, however, it is convenient to ignore the thermal component and to reinterpret the potential-derived part in expression 3.4 in terms of atomic contributions to the total system stress. This goal can be achieved straightforwardly if the empirical potential V has the form of a sum of terms such as 3.1. For two-body interactions, for example, we make use of the fact that the forces exerted on each atom participating in the interaction are equal and opposite to write down

$$\sigma_{\alpha\beta} = \frac{1}{\mathcal{V}} \sum_{j<i} f_{ij\alpha} r_{ij\beta} = \sum_i \frac{\mathcal{V}_i}{\mathcal{V}} \left(\sum_{j \neq i} \frac{f_{ij\alpha} r_{ij\beta}}{2\mathcal{V}_i} \right) \Rightarrow \sigma_{i\alpha\beta}^{atomic} = \sum_{j \neq i} \frac{f_{ij\alpha} r_{ij\beta}}{2\mathcal{V}_i}$$

where $\mathcal{V}_i$ is the atomic volume of atom i. It can set as the average volume per atom in a given system or determined according to the more sophisticated Voronoi tessellation (see section 3.4.2). The subscripts α and β on $f_{ij\alpha}$ and $r_{ij\beta}$ denote Cartesian components of those vectors. In general, we can write

$$\sigma_{i\alpha\beta}^{atomic} = \frac{1}{\mathcal{V}_i} \sum f_\alpha r_\beta$$

where the summation is taken over all forces acting on atom i. This form of the atomic stress is easily applied to three-body terms as well as higher order ones (Brown and Neyertz [1995]).

3.4.2 Atomic strain

In addition to characterizing stresses on the atomic level, it is convenient to be able to define a measure of atomic-level strain. Such a definition was proposed by Mott who made use of the dual Voronoi and Delaunay tessellations of space in his development (Mott *et al.* [1992]). The strain measure described here is essentially Mott's, although with a few modifications.

Given any set of points in a space—call them "atoms"—the Voronoi tessellation subdivides the space into polyhedral regions constructed around individual atoms. These regions have the property that any location within a given region is closer to the atom around which the region is constructed than to any other atom (De Berg *et al.* [2000]). Locations on boundaries between two such regions are equidistant from two atoms. Locations where three such regions meet are equidistant from three atoms. For a general distribution of atoms in space (i.e. for one that lacks any symmetry properties, e.g. a random distribution) there are no points that are equidistant from five or more atoms. Nevertheless, such circumstances can arise in ordered distributions of atoms such as crystal lattices.

Given a Voronoi tessellation of any configuration, it is possible to construct yet another subdivision of space: the Delaunay tessellation. This scheme uses the same principle that was applied to find the Voronoi tesslellation, but with the vertices of the Voronoi tessellation as starting points, i.e. it subdivides space into regions centered on vertices of the Voronoi tessellation such that any location within a region is closer to the vertex around which it is constructed than to any other vertex. This tessellation can be shown to result in a subdivision of space into tetrahedra whose vertices are the atoms of the given configuration for which the original Voronoi tessellation was constructed. A moment's reflection will reveal that since the vertices of the Delaunay tessellation are the original atoms of the configuration, one more application of the principle used to generate

the tessellations described above will once again yield the Voronoi tessellations. The Voronoi and Delaunay tessellations are therefore *dual* (De Berg *et al.* [2000]).

Voronoi and Delaunay tessellations each offer distinct advantages for the purposes of defining an atomic-level strain measure. The polyhedra of the Voronoi tessellation are purely geometrical objects each of which is unambiguously associated with one atom. Furthermore, their shape is uniquely determined for any distribution of atoms. The deformations of Voronoi polyhedra resulting from displacements of atoms in the system are therefore a natural candidate for defining an atomic level strain measure. Their drawback, however, is that these deformations can be highly nonuniform (owing to the potentially nonuniform displacements of the underlying atoms) and the resulting strain measure would have to exhibit a sufficient complexity to reflect these effects. The Delaunay tessellation, on the other hand, yields tetrahedra whose deformations are easily described by uniform strains. It is centered not on atoms, however, but on interstitial regions, i.e. the vertices of the Voronoi tessellation. An ambiguity therefore arises as to the atom to which the strains observed in a Delaunay tetrahedron should be assigned.

Mott's solution to the problem described above was to find the strains for the components of the Delaunay tessellation, but to apportion them to individual atoms making use of the Voronoi tessellation. This assignment was achieved by finding the volume of the intersection between each Voronoi polyhedron and Delaunay tetrahedron. The (nonuniform) strain of each Voronoi polyhedron was then determined as a sum of contributions from all Delaunay tetrahedra that intersected it, each term in the sum being weighted by the previously determined intersection volume:

$$\varepsilon_{\alpha\beta}^{atomic} = \sum \left(\frac{V^{\text{int ersection}}}{V^{atomic}} \right) \varepsilon_{\alpha\beta}^{Delaunay}$$

The initial construction of the Voronoi and Delaunay tessellations was achieved by the method of Tanemura *et al.* [1983] and the apportioning of strains was conducted essentially as described by Mott [1992]. Nonetheless, two important improvements were made. First, as pointed out earlier, for general distributions of atoms it is very unlikely that there should exist points equidistant from four (five, for 3-D) or more atoms. If such

a "degenerate" situation should arise, it would correspond to five or more Voronoi polyhedra meeting at a single vertex. The amorphous structures under study here are sufficiently disordered for degenerate situations to arise very rarely, but regions of local partial crystallinity are nonetheless possible. In such cases, the original algorithm fails. The modification introduced for the purposes of the current research circumvents this problem by recognizing the degenerate situations described above and arbitrarily choosing from among the number of equivalent configurations that are made possible by it (Tanemura *et al.* [1983]).

The second improvement concerns the method of finding intersections between Delaunay tetrahedra and Voronoi polyhedra. Whereas Mott used a recursive method that defined the total intersection volume iteratively as a sum of successive terms, the method used here determines the intersections directly by finding the region bounded by all surfaces of both the Voronoi polyhedron and Delaunay tetrahedron of interest. It therefore avoids all possible problems of convergence. It was found that Mott's implementation frequently failed to give consistent outputs even when the initial tessellation was successful. The improved scheme failed only once out of the almost one thousand times that it was applied.

3.4.3 Hydrostatic and deviatoric tensor components

The methods for finding atomic level stresses and strains described above yield a full tensorial description of these quantities. For the purposes of analysis, however, it is usually convenient to find scalar quantities that by themselves characterize certain aspects of the full tensor. Two such scalars are of particular interest: the hydrostatic and equivalent deviatoric components. Given any tensor A they are

$$A_{hyd} = \tfrac{1}{3} tr(A)$$
$$A_{dev} = \sqrt{tr\left(\left(A - A_{hyd}\right)^T \left(A - A_{hyd}\right)\right)}$$

These scalars have particular significance in the context of mechanical deformation of materials. The negative hydrostatic component of the stress tensor is the system pressure.

Similarly in the case of strain, the hydrostatic component corresponds to dilatation. Meanwhile, the $\sqrt{\frac{2}{3}}$ times the deviatoric component of stress is the von Mises stress often used in yielding criteria (McClintock and Argon [1966]).

4. Results

This section describes the results of MD and CGSEM simulations carried out in the course of the investigation. All results pertain to systems containing 4096 atoms. In order to eliminate any possible surface effects, all simulations were conducted under periodic boundary conditions.

4.1 Creating a-Si

The available methods that attempt to create computer models of a-Si with a continuous random network structure can be broadly classified into two categories: direct construction by bond switching (Wooten *et al.* [1985]) and melting and quenching (Luedtke and Landman [1989]). The former starts with a diamond cubic crystalline sample and progressively disorders it by rearranging individual bonds according the pre-specified rules. Although effective for small system sizes, this method becomes cumbersome when thousands of atoms are involved. Furthermore, the bond-switching process is inherently unphysical as no instance of such "self-amorphization" at low temperatures has been observed in silicon.

a-Si creation by melting an quenching, on the other hand, has been known at times to produce final structures whose character was further from the anticipated continuous random network than when bond switching was used (Luedtke and Landman [1989]). Nevertheless, the way in which melting and quenching arrives at the amorphous configuration is more true to the way a-Si could be made in an experimental setting. Therefore, the approach used in the present research was the melting and quenching approach.

4.1.1 Initial condition: c-Si

Melting and quenching was accomplished by using a constant temperature molecular dynamics (MD) algorithm. The initial conditions provided for the simulation were the positions of atoms in a perfect diamond cubic silicon crystal. This initial system configuration was constructed in such a way that all atoms were stationary and in equilibrium (corresponding to zero temperature). The size and shape of the simulation cell was chosen in such a way as to minimize the overall system potential energy (corresponding to zero stress).

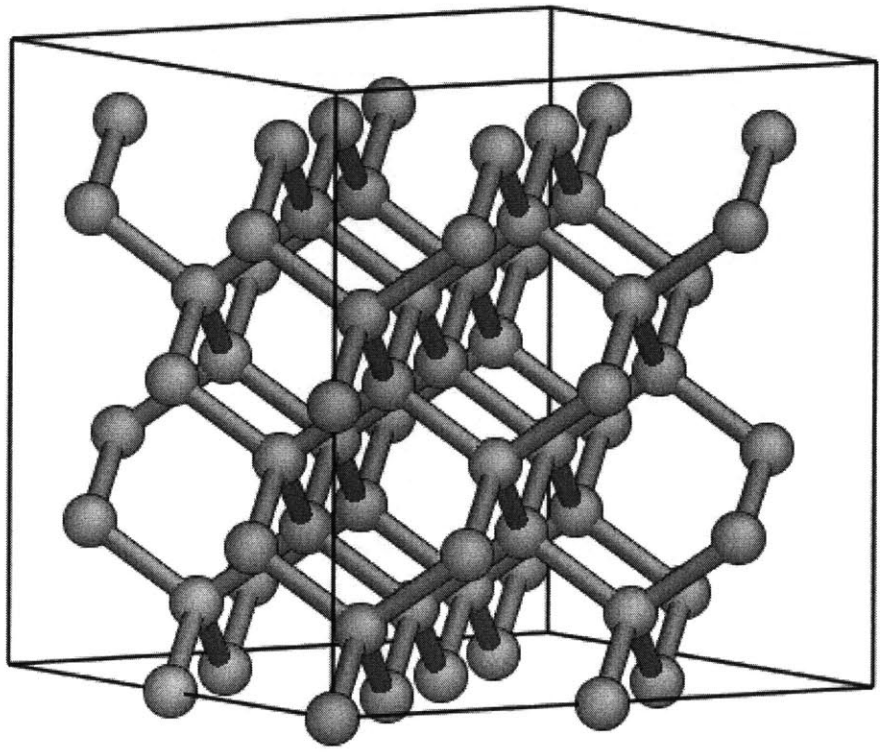

Figure 4.1: The configuration of atoms in the diamond cubic crystal structure. In the Stillinger-Weber potential for silicon, the equilibrium distance between nearest neighbor atoms (i.e. the bond length) in this configuration is 0.235nm.

The diamond cubic structure can be described in terms of cubic unit cells—each containing eight atoms—repeating in the x, y, and z directions. Although this cubic cell is not the primitive cell (the primitive unit cell is similar to the one for the FCC configuration, but contains two atoms (Ziman [1995])), it is convenient for the purposes of both constructing and visualizing a crystalline silicon (c-Si) configuration. Figure 4.1 illustrates the arrangement of atoms in the diamond cubic crystal structure. It is easy to see that in this configuration each atom has four nearest neighbors, i.e. diamond cubic c-Si is four-fold coordinated.

4.1.2 Melting

The initial crystalline structure described above was melted by conducting MD simulations at increasing temperatures. Starting at T=25K, the temperature was increased by increments of 25K up to T=4000K. At each temperature, the structure was equilibrated for 2000 MD time increments (a total of 10.7 ps), corresponding to 140 atomic vibration periods in the Stillinger-Weber potential. The rate of temperature increase was therefore $2.33 \cdot 10^{12}$ K/s, i.e. much higher than can normally be achieved experimentally (with the possible exception of pulsed laser melting (Thompson *et al.* [1984])). Conducting the melting process at lower rates of temperature increase did not, however, yield any changes in the observed melting profile. This insensitivity to heating rate can be explained by lack of temperature-activated relaxation processes in the crystalline state and the very fast thermodynamic equilibration of atomic positions in the liquid state.

The dependence of system specific volume (volume normalized by the volume of c-Si at zero temperature and stress) during melting is shown in figure 4.2. The most prominent feature of this profile is the sudden drop of volume at a temperature of about 2500K. This volume drop coincides with the melting of the crystalline configuration and is characteristic not only of silicon, but also generally of many substances that exhibit a diamond cubic crystalline structure (Angell *et al.* [1996]), the best known of these being water. Indeed, obtaining a drop in volume upon melting was one of the central

motivations behind the choice of parameters for the Stillinger-Weber potential (Stillinger and Weber [1985], see section 3.1).

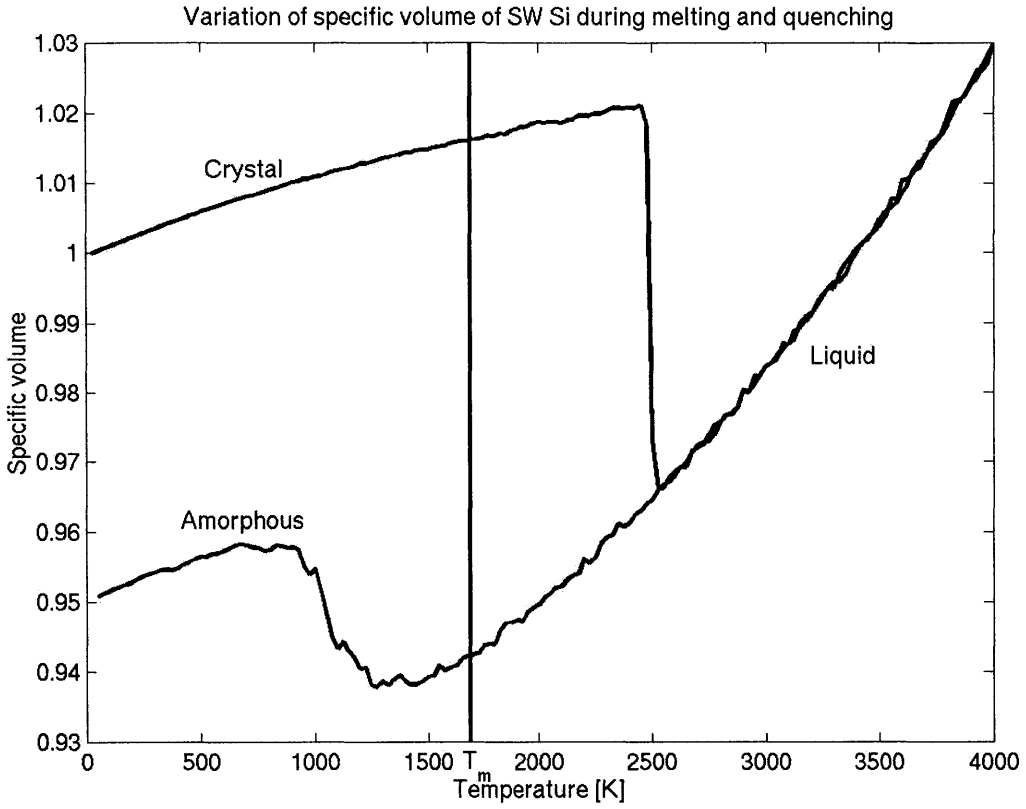

Figure 4.2: c-Si contracts upon melting and—given a high quench rate—does not recover all of the lost volume upon vitrification.

Although melting of c-Si in a MD simulation such as the one described here occurs at about T=2500K, this is not the phase transition temperature between the crystalline and molten state, i.e. it is not the thermodynamic melting temperature T_m. Broughton and Li showed that T_m for the Stillinger-Weber potential is 1691 ± 20K (Broughton and Li [1987]). Because, however, the initial crystalline arrangement in the simulation described here was flaw-free, the system could undergo a high degree of overheating due to the large barrier to nucleating an initial molten region. Defects such as grain boundaries can serve as preferred sites for easy nucleation of the melt. Indeed, if such defects are introduced into the initial configuration, the temperature at which the

system undergoes melting is drastically decreased and approaches T_m (Phillpot *et al.* [1989]).

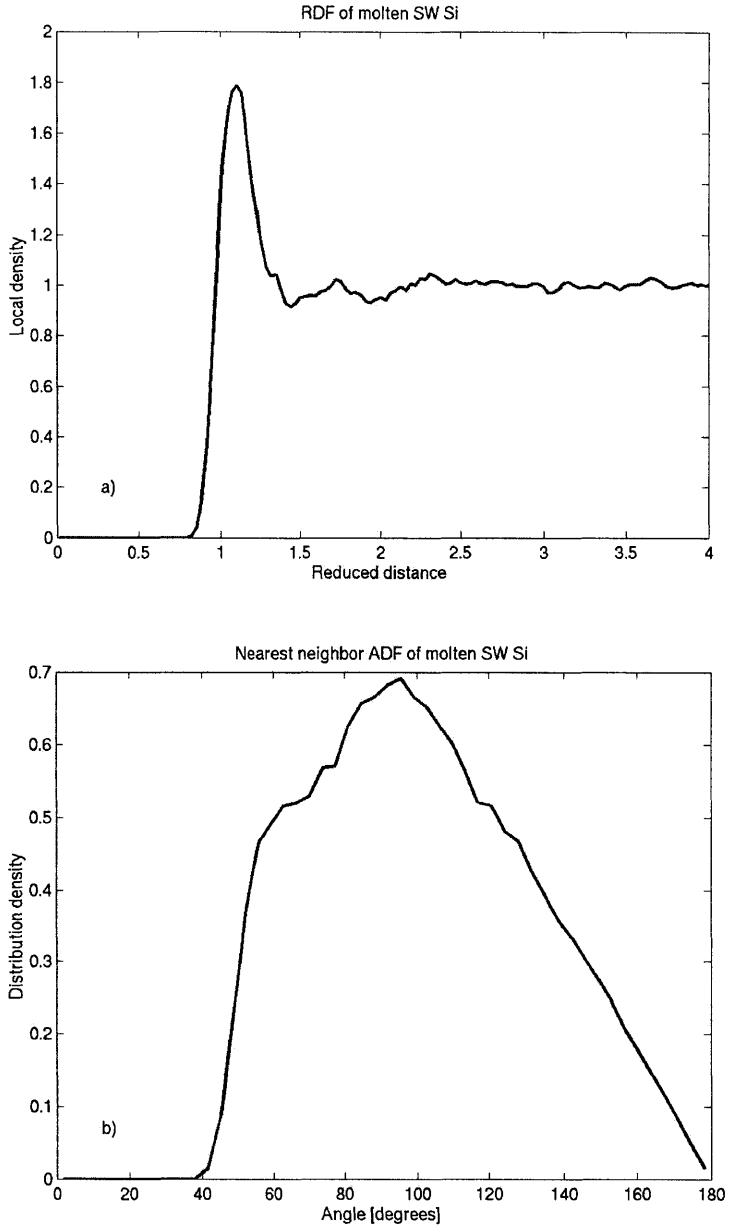

Figure 4.3: a) RDF of molten silicon. Distances have been normalized by the Stillinger-Weber characteristic distance (section 3.1). B) ADF of molten silicon.

Evaluation of radial and angular distribution functions (RDFs and ADFs) for molten silicon clearly shows the disappearance of long range order as well as a loss of definition in the bond angles between nearest neighbors (fig. 4.3). By integrating the RDF

up to the first "trough" after the nearest neighbor peak we can conclude that the average coordination of molten Si as modeled by the Stillinger-Weber potential is around 6, which is in good agreement with the experiment (Davidovic *et al.* [1983]).

4.1.3 Quenching

Upon reaching T=4000K, the temperature of the system was decreased in 25K increments and the system configuration was equilibrated by MD simulation at each new temperature in the same way as was described above. The resulting variation of specific volume during quenching is depicted in figure 4.2. The system persists in the molten state for temperatures far below the melting temperature and eventually vitrifies at T_g: the glass transition temperature. Subsequent heating of the vitrified material leads to remelting at the glass transition temperature.

The phenomenon of undercooling is analogous to the overheating described above in that a transition to the thermodynamically stable state (the crystalline state, in this case) is impeded by a nucleation barrier. Much as this nucleation barrier can be reduced in the case of melting by the insertion of defects into the crystal structure, it can be eliminated in the case of crystallization if a small crystalline nucleus is added at a temperature slightly below T_m. The molten material surrounding it then crystallizes on time scales accessible to MD simulation (Keblinski *et al.* [1996a, 1996b]). The time scale for the spontaneous creation of such a nucleus, however, is prohibitive given current computational capabilities unless specially modified empirical potentials are used (Nakhmanson and Mousseau [2002]).

Increasing degrees of overheating lead to the crystalline structure to become increasingly unstable under thermal motion resulting in an eventual spontaneous transition to the molten state (Phillpot *et al.* [1989]). Increasing degrees of undercooling, however, are accompanied by ever decreasing atomic mobilities making it more difficult for crystalline nuclei to form and grow. Eventually, atomic mobilities become so low that the underlying liquid configuration becomes "kinetically frozen" and no longer undergoes significant structural relaxation. The temperature at which this phenomenon occurs is called the glass transition temperature T_g and is easily identified by the rapid

change in thermal expansion coefficient of the material. Note from figure 4.2 that the thermal expansion behavior of the material is nearly identical before melting and after glass transition: thermal expansion coefficients for the crystal and glass are $\alpha_{c-Si} = 1.26 \cdot 10^{-5} K^{-1}$ and $\alpha_{a-Si} = 1.14 \cdot 10^{-5} K^{-1}$, respectively. The thermal expansion coefficient of the liquid, however, is nearly four times higher: $\alpha_{l-Si} = 4.18 \cdot 10^{-5} K^{-1}$.

Unlike the melting phase transition from crystal to liquid structures (Huang [1987]), the exact physical nature of the glass transition is not yet well understood.

4.1.4 Structure characterization

Much like in the case of metallic glasses, the character of amorphous silicon as formed by melting and quenching depends sensitively on the rate of quenching: slow quenching allows for greater structural relaxation resulting in a disordered configuration whose macroscopic features (e.g. specific volume) more closely resemble that of the crystal. Fast quenching, on the other hand, locks in a less-relaxed configuration whose characteristics are less like those of the crystal. Figure 4.4 shows the effect of increasing the quench rate from $2.33 \cdot 10^{12}$ K/s to $3.73 \cdot 10^{13}$ K/s on specific volume variation in Stillinger-Weber a-Si. Unlike in the case of metallic glasses, slower quenching leads to a rise in the specific volume of the product. Nevertheless, since silicon in its molten form is denser than the crystal, this rise in specific volume is consistent with slowly quenched glasses being more structurally relaxed and therefore more similar to the crystal structure than those that were quenched quickly.

Because structural features of a-Si are not readily appreciable by inspection, atomic-level differences between quickly and slowly quenched a-Si were investigated by numerical means. Figure 4.5 compares the RDFs and ADFs of the quickly and slowly quenched a-Si structures with those of c-Si. Note that in both cases long-range order is lost and bond angles are widely dispersed (although less so than in the case of molten silicon, see figure 4.3). The split second peak apparent in the RDFs of both structures indicates that second nearest neighbors are ill defined in the system (Zallen [1979]). This characteristic of the RDF is a feature commonly observed in equilibrated ball bearing

packings and metallic glasses. Its presence in the RDFs of a-Si is a sign that some residual structural characteristics of the (metallic) liquid form of silicon remain in the system even after the glass transition.

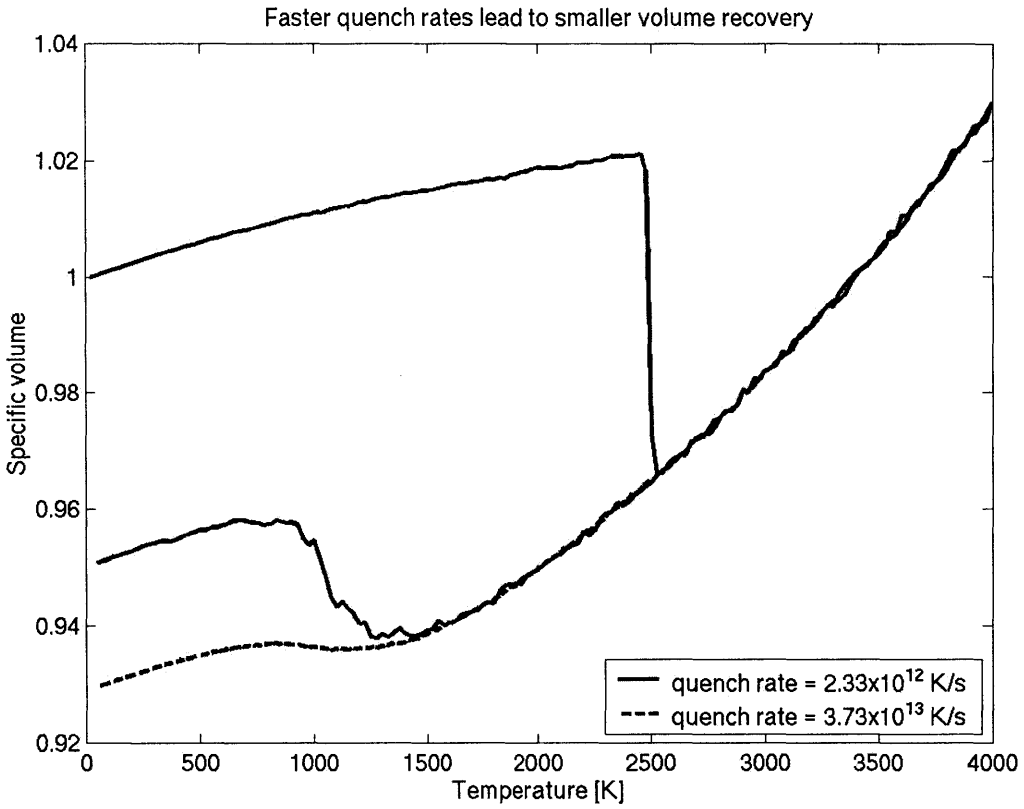

Figure 4.4: The faster molten silicon is quenched, the denser the final amorphous structure.

In the continuous random network setting, no split second peak is expected (Zallen [1979]). It is not surprising, therefore, that the structure of the more slowly quenched system is in better agreement with experiment (Laaziri *et al.* [1999]). Integration of the RDFs up to the first trough after the nearest neighbor peak shows that the average system coordination of the quickly quenched structure is 4.6 while that of the slowly quenched structure is 4.4. In this respect the slowly quenched structure is once again in better accord with experiment.

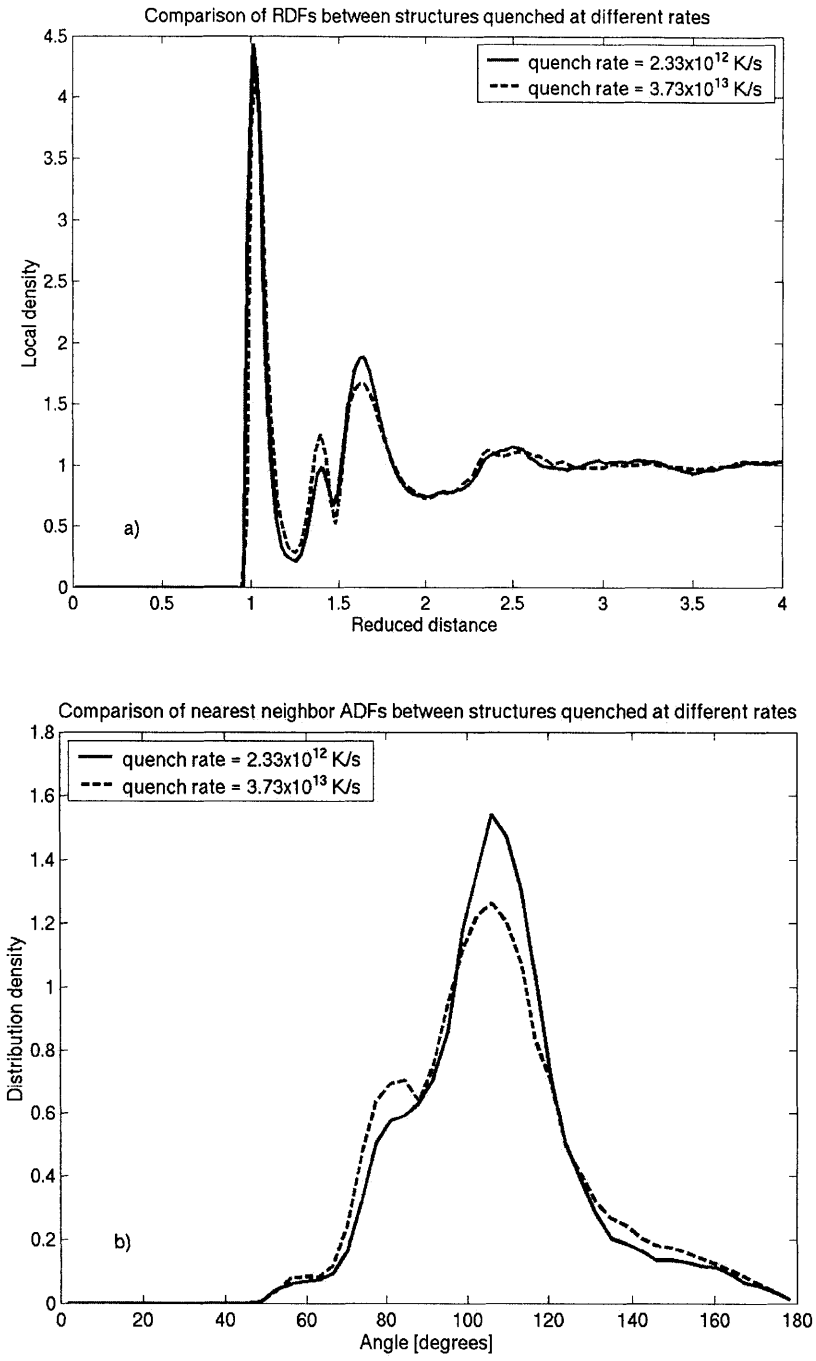

Figure 4.5: a) The split in the second neighbor peak is less pronounced in the more slowly quenched structure. b) The bond angles in the more slowly quenched structure are less dispersed than in the more quickly quenched one.

4.2 Irreversible deformation: system view

After a-Si structures were created using the melting and quenching process described above, the best relaxed of them was deformed plastically by using conjugate gradient static energy minimization (CGSEM) simulations. This section describes the system-wide response of the material to such deformation.

4.2.1 Loading procedure

a-Si structures containing 4096 atoms and generated by the quenching process described in section 4.1 were brought to the closest equilibrium configuration (corresponding to zero temperature) by minimizing the system potential energy using the CGSEM method (section 3.3). Next, in order to deform such equilibrated structures, strain increments were successively imposed on the system by changing the shape of the simulation cell. These strain increments were chosen such that they did not change the system volume and did not allow for any deformation in the z-direction. Therefore, they can be described as increments of volume conserving plane strain (figure 4.6).

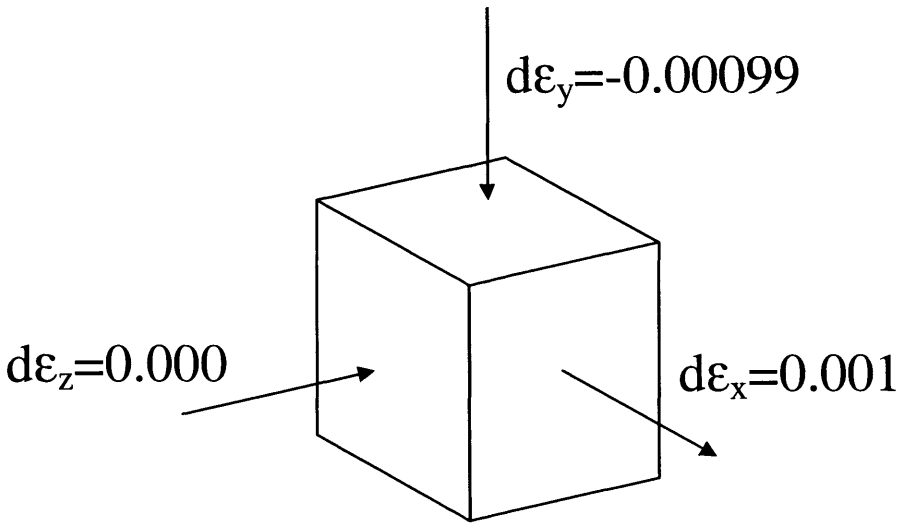

Figure 4.6: The system was loaded with volume conserving plane strain increments.

After an increment of strain is imposed on the system, the resulting atomic arrangement is in general no longer in equilibrium. Therefore, after each strain increment the CGSEM algorithm was used to once again bring the system into the closest equilibrium configuration. The process of successively deforming and reequilibrating an a-Si system can be carried out repeatedly to generate a large-strain deformation profile.

4.2.2 Discrete stress relaxation events

If small increments of strain are applied to a system consisting of a few thousand atoms, then a smooth variation of system pressure and deviatoric stress is observed. Now consider that the deformed system is unloaded, i.e. that the CGSEM-based deformation process described above is repeated except using strain increments that are inverse to the ones used when initially deforming the system. Such deformation eventually returns the simulation cell to its initial shape. For such unloading the system pressure and deviatoric stress are seen to retrace the values they took in the case of initial loading (figure 4.7). Therefore, when the system stress-strain response is smooth, the deformation is reversible by simple unloading and can therefore be considered elastic.

If, on the other hand, a discontinuous change in the system stress is observed during loading, the unloading behavior of the system becomes entirely different as figure 4.7 illustrates. The stress-strain behavior is clearly irreversible. Meanwhile, differences in atomic positions between the system configuration for loading and for complete unloading following the stress-strain discontinuity show that the system has suffered an internal structural change that cannot be reversed by simple unloading (figure 4.8).

The stress relaxations described here have been observed before in deformation simulations of a variety of disordered materials (e.g. Argon and Shi [1983]; Mott *et al.* [1993]). They have been identified as indicators of discrete atomic-level mechanisms responsible for system plastic deformation. The apparently smooth macroscopic stress-strain behavior of materials undergoing plastic deformation is thought to be a result of the ensemble-averaging of large numbers of unit events like the one shown in figure 4.7.

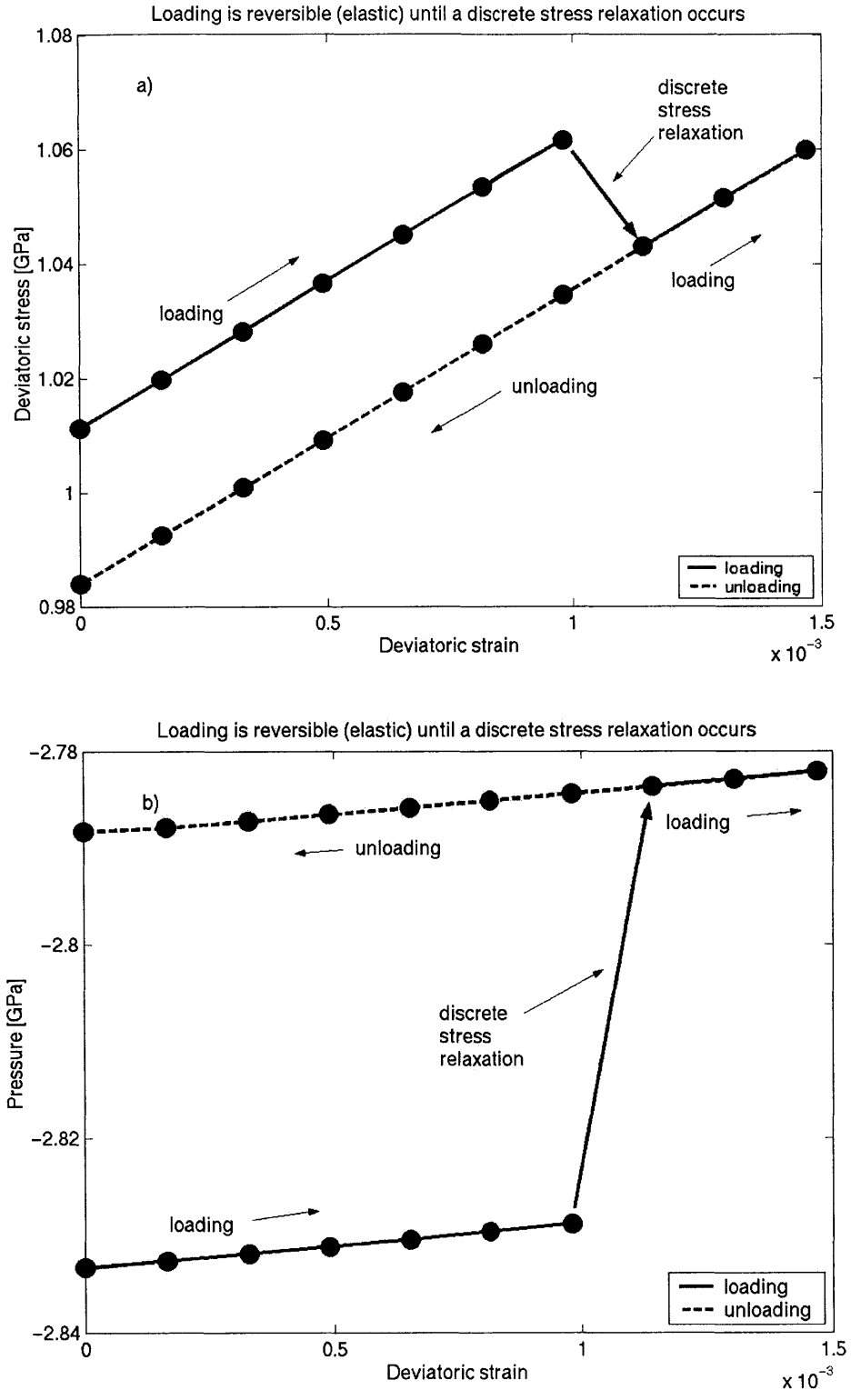

Figure 4.7: Discrete a) deviatoric stress and b) pressure relaxations are not reversible upon unloading. Circles on lines represent values from individual system configurations.

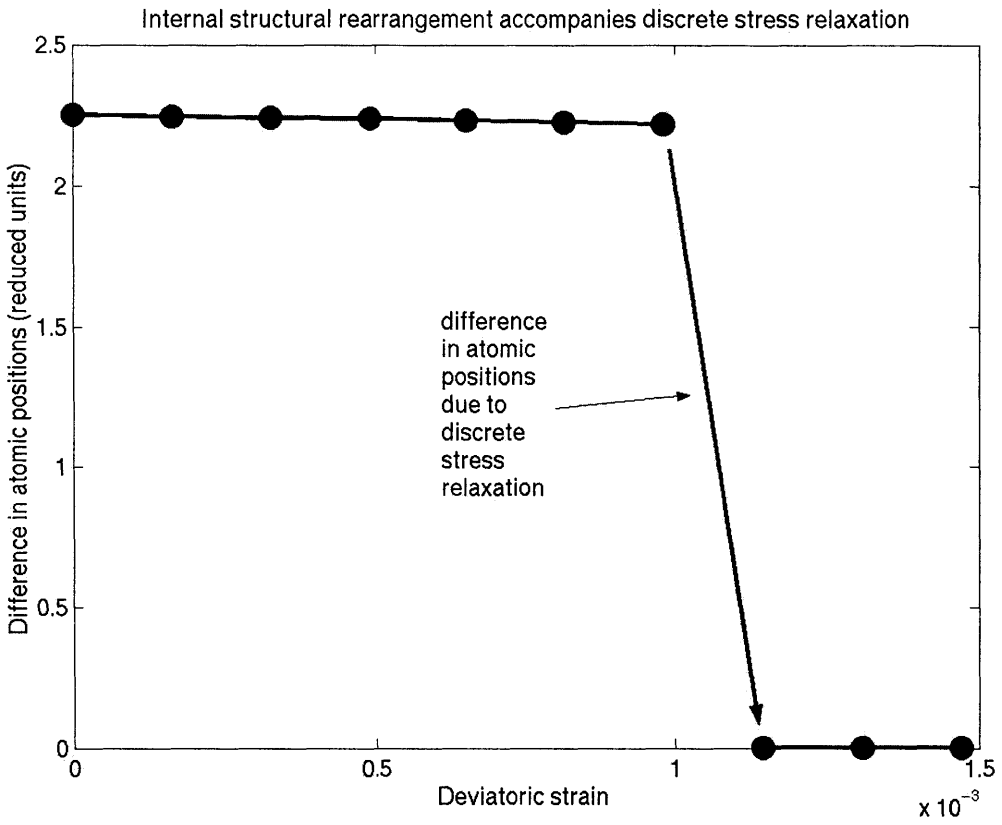

Figure 4.8: Comparing positions of atoms in a-Si samples that are similarly strained but correspond to the loading and unloading branches of figure 4.7 reveals that an internal structural rearrangement accompanies the discrete stress relaxation. Distances are normalized by the characteristic length of the Stillinger-Weber potential (section 3.1).

4.2.3 Deformation to large strain

If a large number of strain increments is applied to an a-Si system, multitudes of discrete stress relaxations such as those described in section 4.2.2 are observed. From the aggregation of these stress relaxations, certain characteristics of the material's macroscopic plastic deformation behavior become immediately recognizable (figures 4.9 and 4.10).

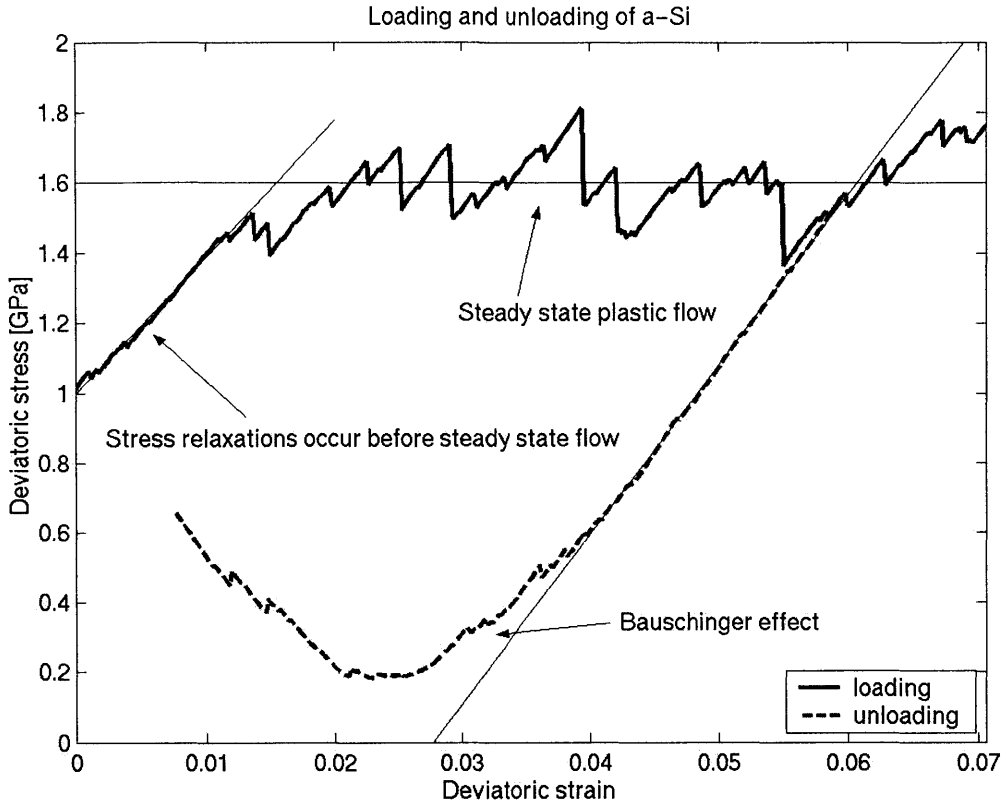

Figure 4.9: The system-wide loading and unloading behavior of a-Si is an "ensemble average" of individual irreversible stress relaxation events.

The variation of deviatoric stress with loading (figure 4.9) clearly illustrates the eventual attainment of a steady state flow state corresponding to plastic flow. No distinct yielding point can be discerned, however, because of the small stress relaxation events that occur even far below the level of deviatoric stress reached at steady state flow. Unloading reveals a clear Bauschinger effect, indicating that residual backstresses are accumulated in the system during plastic deformation. A state of zero deviatoric stress is not reached upon unloading because of the pronounced effect of atomic level stress variations on the overall system stress in an a-Si structure this small in size.

The interpretation of variation of system pressure with loading and unloading (figure 4.10) proves to be more problematic than the interpretation of variation in deviatoric stress. In particular, while the latter reaches a steady state flow condition at a deviatoric strain level of about 1-2%, the former never attains steady state. Furthermore, a

distinct asymmetry exists between the pressure profiles for loading and unloading. The explanation of these issues is a topic in the author's doctoral research.

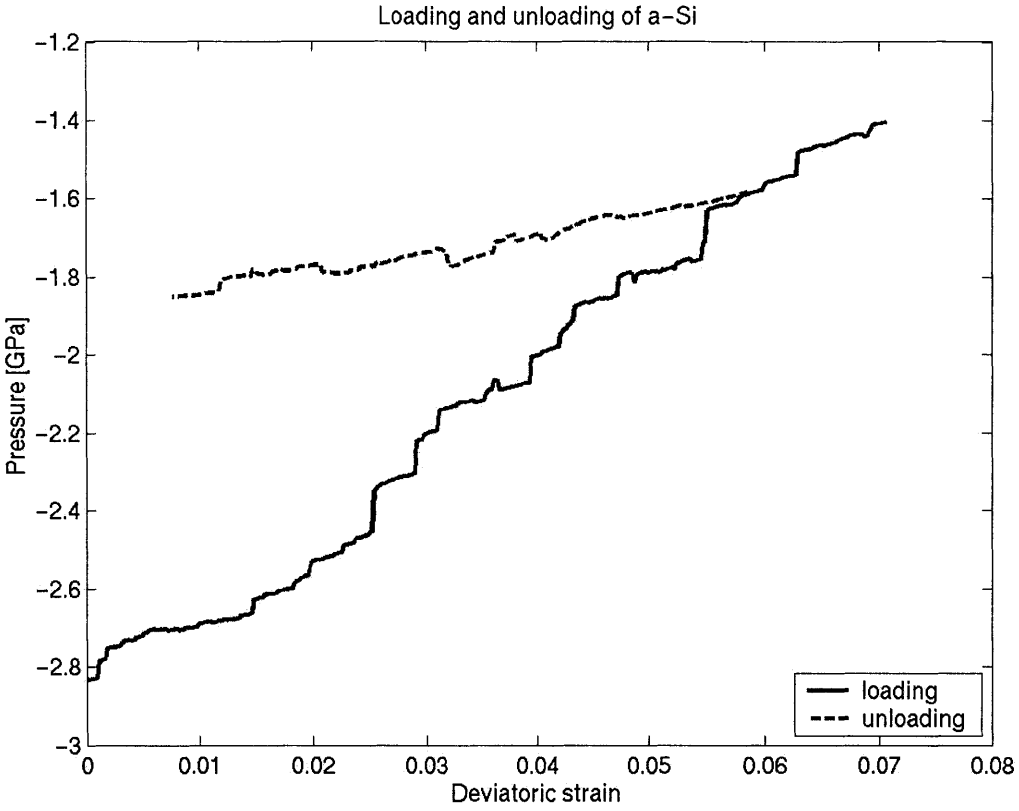

Figure 4.10: The system pressure profile fails to achieve steady state even after the deviatoric stress profile has achieved it.

4.3 Irreversible deformation: atomic level

Discrete stress relaxations have been shown to reproduce the macroscopic stress-strain features of plastic response. These events were accompanied by irreversible internal structural changes. In this section we clarify the nature of the collective atomic rearrangements that accompany discrete stress relaxation events.

4.3.1 Kinematics of transformation

The method for finding atomic level strain increments described in section 3.4.2 can be applied to any two system configurations. Once a set of atomic strain increments

is found, the hydrostatic and deviatoric components can be computed (section 3.4.3). Since plastic deformation in other disordered materials was found to be a localized shearing process (section 2.3), the atomic deviatoric strain increment can be viewed as a good measure of the intensity of a given atomic environment's contribution to the structural rearrangement accompanying discrete stress relaxation.

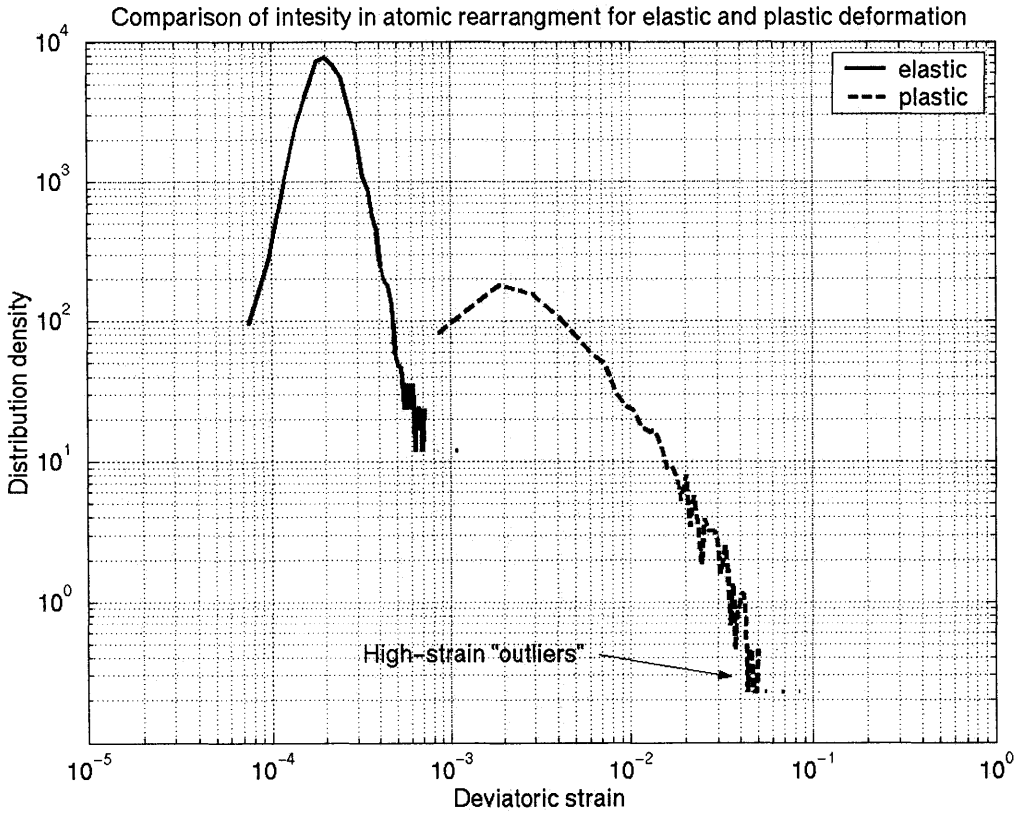

Figure 4.11: Atomic deviatoric strain increments are much higher for a-Si configurations undergoing stress relaxation than for those being deformed elastically. Distributions have been normalized to unity.

Figure 4.11 shows distributions of atomic deviatoric strain increments computed for a pair of structures that are elastically (reversibly) deformed versions of each other as well as for a pair of which one corresponds to a configuration immediately preceding and the other immediately succeeding a stress relaxation. The atomic deviatoric strains in the latter are on average larger than those in the former by about two orders of magnitude. Moreover, while the deviatoric strains of the majority of atoms fall into the low-strain regime ($<10^{-2}$), there is a small number of atoms whose deviatoric strains are much larger

than of the rest. These "outliers" in the atomic deviatoric strain distributions indicate atomic environments where atomic rearrangement is concentrated during a stress relaxation.

4.3.2 Visualization of transformation

The analysis of section 4.3.1 can be used in visualizing the geometrical character of individual stress relaxations. Figure 4.12 shows a cluster of atoms containing only atoms of highest deviatoric strain increment for a pair of a-Si configurations corresponding to a stress relaxation. Clearly, the atomic rearrangements during discrete plastic deformation events are highly localized in a well-defined region of space.

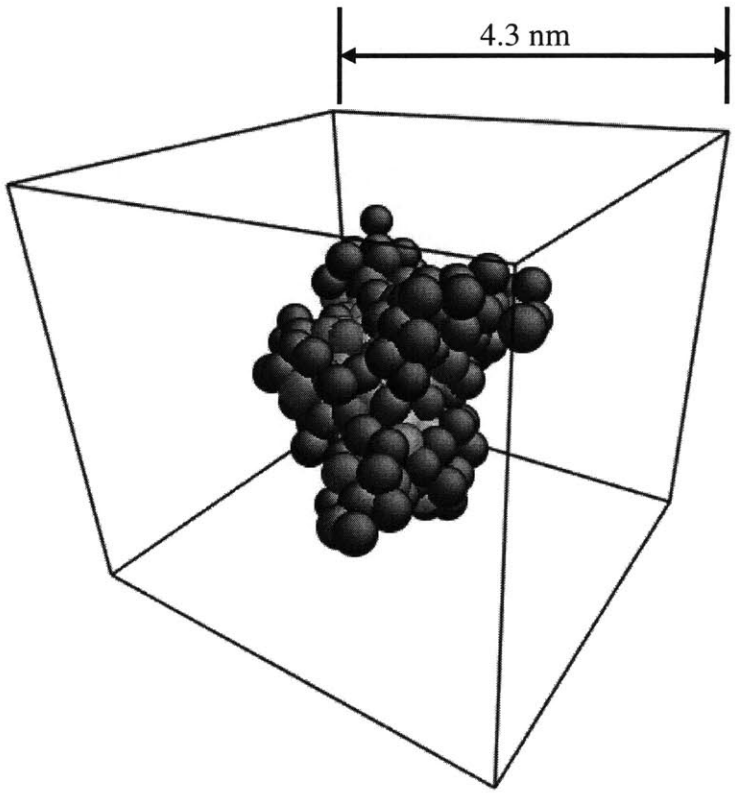

Figure 4.12: Atoms whose environments undergo the largest deviatoric strain increment during a plastic stress relaxation are well localized within the system configuration.

Figure 4.13 is a visualization of the region of highest atomic rearrangements for a stress relaxation in a system of 1000 atoms (as opposed to the 4096 used in all other

situations). Here the deformation is also highly localized, but it is not contained within a closed region. Instead, it connects across the periodic boundary walls of the simulation cell. This phenomenon is due to the excessively small system size and the strength of the resulting elastic fields generated by periodic images of regions where deformation localized. It has been observed before in glassy polymers (Mott *et al.* [1993]).

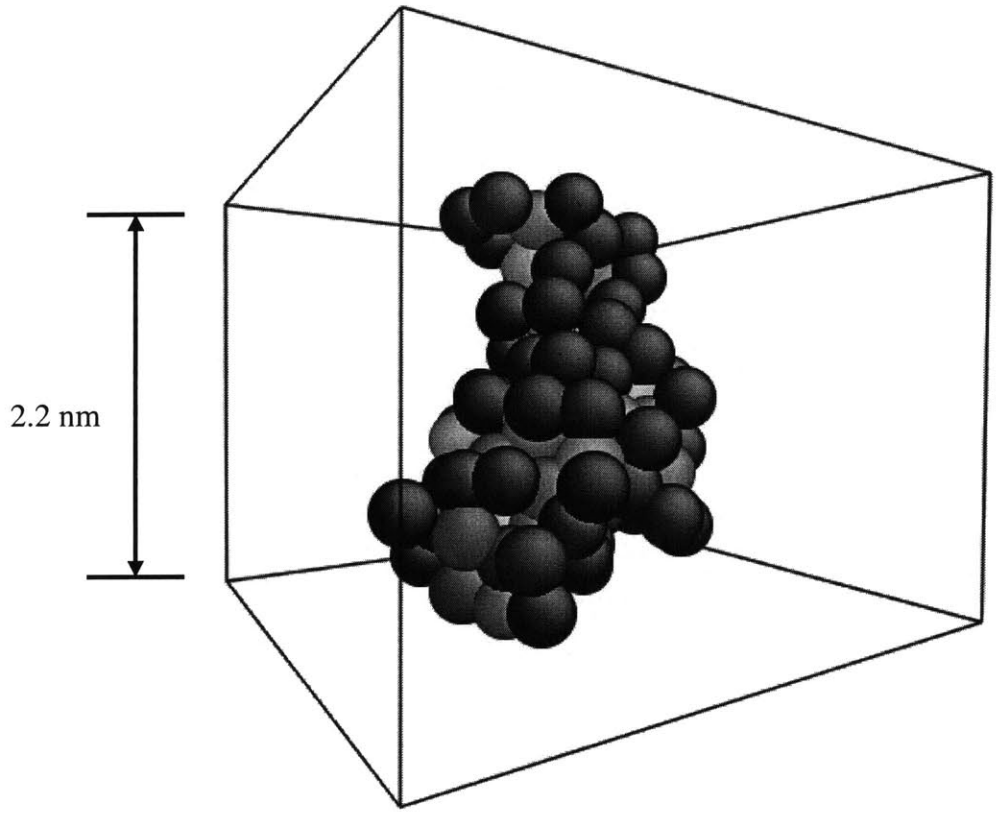

Figure 4.13: For a system consisting of 1000 atoms, regions of highest shearing during plastic stress relaxation connect across periodic boundary walls.

This connecting across periodic boundary walls of plastically transforming regions was the motivating reason behind choosing a larger, 4096-atom system for the research presented here. The atomic deviatoric strain increment characterization of the kinematics of plastic transformation is therefore a useful tool in not only visualizing the nature of atomic rearrangements accompanying discrete stress relaxation, but also provides a means for detecting artifacts resulting from system size effects and the accompanying elastic image forces.

4.3.3 Analysis

Characterization based on atomic deviatoric strain increments allows for the visualization of transforming regions and the extraction of qualitative information. A more quantitative account of the kinematics of plastic deformation, however, requires making an objective choice for the cutoff atomic deviatoric strain increment below which atomic environments are not seen as participating in the rearrangements leading to discrete stress relaxation. This choice was made individually for each event based on the variation with the cutoff deviatoric strain of the stresses and potential energy per atom associated with the transforming region.

By choosing a cutoff atomic deviatoric strain increment, a certain number of atomic environments are marked as being within a transforming region while the other ones are considered to be outside it. The stresses and potential energies per atom of these regions can then be evaluated. As the cutoff deviatoric strain increment decreases, the number of atoms participating in a transformation increases. Thus—via the cutoff deviatoric strain increment—a correspondence can be drawn between the number of atoms participating in an irreversible rearrangement and the stresses and potential energies per atom associated with that rearrangement.

Figure 4.14 plots the number of atoms against the differences in pressure and potential energy per atom for a typical pair of a-Si structures associated with a discrete plastic event. For small numbers of participating atoms, the pressure and potential energy per atom differences vary erratically. For large numbers, however, the variation dies down. A certain "participation number" of atoms can be chosen that separates the regime of erratic variation of pressure and potential energy per atom differences from their smooth behavior. This participation number is an estimate for the size of the transforming regions. For the relaxations observed, it was found to lie between 100 and 500 atoms per event.

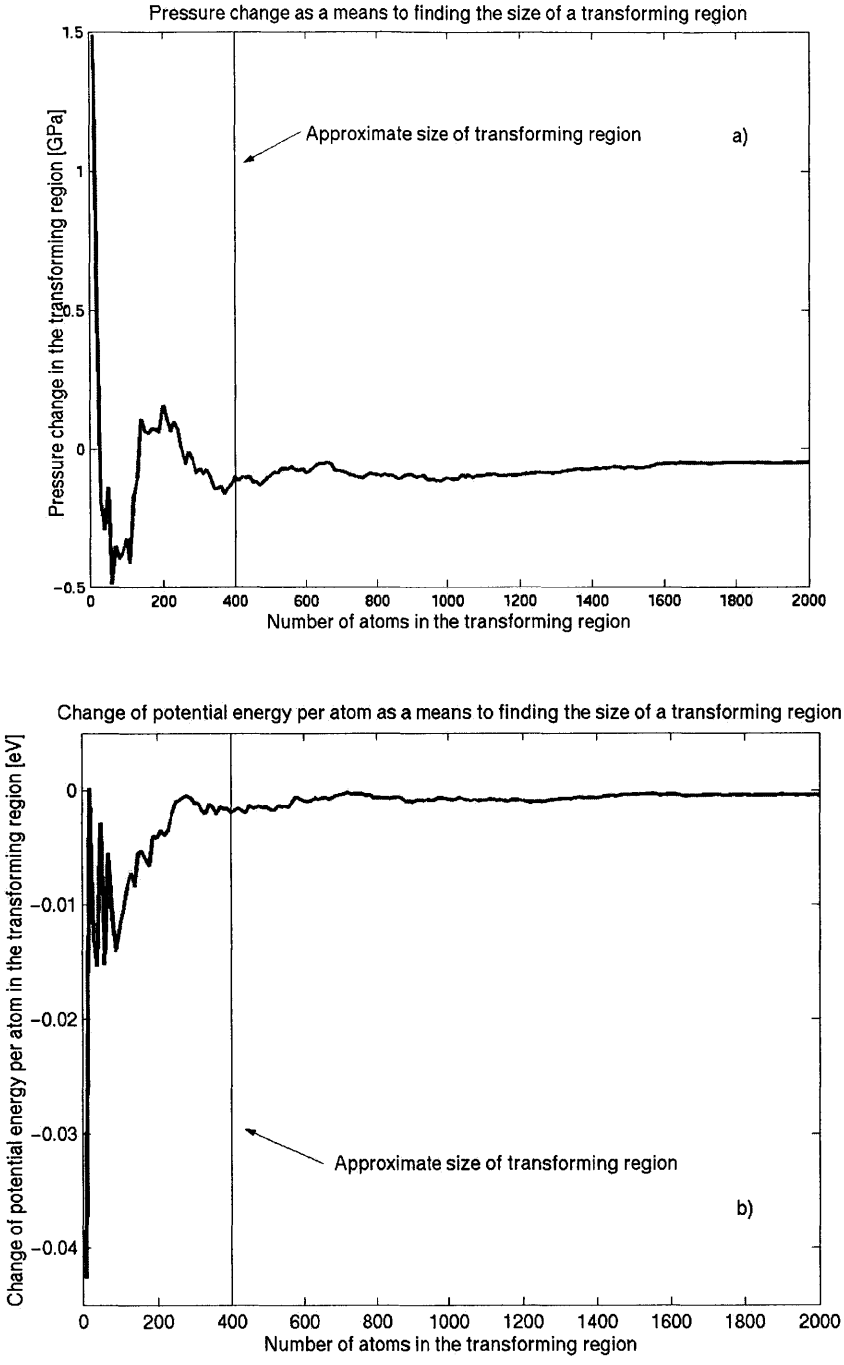

Figure 4.14: Differences in a) pressure and b) potential energy per atom inside a transforming region between the atomic configuration immediately before and after a plastic stress relaxation help to determine the size of the transforming region. Atoms with environments of highest deviatoric strain increment are included in the transforming region first. The region is then enlarged by including atomic environments of ever lower deviatoric strain increments. The size of the transforming region is taken to be the number of atoms at which pressure and potential energy per atom differences cease to vary erratically.

With an estimate for the size of transforming regions and the degree of the accompanying deviatoric and hydrostatic stress relaxation, the distribution of deviatoric and hydrostatic transformation strains for discrete relaxation events can be found. We use the formulas (Argon [1996])

$$\Delta\varepsilon_{dev}^{event} = \frac{N^{system}}{N^{event}} \cdot \frac{\Delta\sigma_{dev}^{system}}{\mu}$$

$$\Delta\varepsilon_{hyd}^{event} = \frac{N^{system}}{N^{event}} \cdot \frac{\Delta\sigma_{hyd}^{system}}{B}$$

where $B = 106GPa$ and $\mu = 33GPa$ are the bulk and shear moduli of SW a-Si, respectively (Kluge and Ray [1988]). N denotes the number of atoms in a given collection. Deviatoric transformation strains were found to be distributed between 0.01 and 0.35. Hydrostatic strains fell into the –0.7-0.1 range.

The localization of atoms that are highly active in a plastic rearrangement process within a well-defined region of space (figure 4.12) lends itself well to approximating that region of space as an ellipsoid (as has been done before in continuum models of plastic transformation (Argon and Shi [1982])). Such an approximation allows for a quantitative characterization of the dimensions of the region along its principal directions as well as of its orientation with respect to the applied stress field.

The approximation described above was made by matching the moment of inertia of a transforming region with the moment of inertia of a similarly oriented ellipsoid. Once the atoms participating in a plastic transformation were determined, the components of the inertia tensor for that region were found according to the formula

$$I_{jk} = \sum_{i=1}^{N} m_i \left(r_i^2 \delta_{jk} - x_{i,j} x_{i,k} \right) \qquad 4.1$$

where N is the number of participating atoms. m_i and r_i are the mass and distance from the origin of atom i. $x_{i,j}$ is the j-component of the i^{th} atom's position. The full inertia tensor for a transforming region was diagonalized to extract the orientation of the region

in the ellipsoid approximation. For the events analyzed, however, no preferential orientation was found.

The diagonal form for the inertia tensor of an ellipsoid with semi-axes denoted by a_x, a_y, and a_z is

$$I_x = \frac{M}{5}\left(a_y^2 + a_z^2\right)$$

Similar expressions hold for I_y and I_z. These relations can be inverted to give the semi-axes of an ellipsoid with principal moments I_x, I_y, I_z:

$$a_x = \sqrt{\left(\frac{5}{2M}\right)\left(I_y + I_z - I_x\right)}$$

Thus, the diagonal elements of the inertia tensor for a transforming region (calculated according to 4.1) can be used to find an "equivalent oriented ellipsoid" that provides an estimate for the length scale and shape of that region. It was found that these equivalent oriented ellipsoids generally had the shape of filaments, i.e. they had one long semi-axis and two shorter semi-axes of equal length. The former had lengths in the interval 1.0-2.5nm and the latter in the interval 0.7-1.8nm.

5. Conclusions

The computer investigation of plastic deformation in amorphous silicon presented here has yielded the following results:

- Plastic deformation occurs as a series of discrete stress relaxations, much as has been observed in glassy metals and polymers.
- Individual stress relaxations are accompanied on the atomic level by highly localized shearing events involving 100-500 atoms and occurring within roughly ellipsoidal regions.
- The length scales involved in the kinematics of atomic rearrangements appear to be within the 0.7-2.5nm range.

The findings presented here have important consequences in the study of irreversible deformation in highly confined covalently bonded intergranular material. In particular, since the thickness of such confined films is in the 0.2-1nm range, it can be concluded that the mechanism responsible for plastic deformation in bulk amorphous covalently bonded materials cannot operate in such a setting.

6. Acknowledgements

The author would like to acknowledge the invaluable contribution made by Ali S. Argon to the research presented here. Without his wisdom, experience, intuition, and constant guidance none of it would have been possible.

For their tutelage, insights, and technical expertise the author would like to acknowledge N. Hadjiconstantinou, V. Yamakov, D. Wolf, J. Li, S. Yip, D. Parks, M. Bazant, N. Marzari, and L. Anand. My gratitude is also due to R. Sharma and M. Zimmermann for countless discussions.

7. References

Abell, G. C., 1985, Phys. Rev. B31, 6184

Allen, M. P., and Tildesley, D. J., 2000, Computer Simulation of Liquids, Oxford University Press, Oxford, England

Angell, C. A., Borick, S., Grabow, M., 1996, J. Non-cryst. Sol. 205-207, 463

Argon, A. S., and Kuo, H. Y., 1979, Mat. Sci. Eng. 39, 101

Argon, A. S., 1981, in Dislocation Modelling of Physical Systems, ed. Ashby, M. F., Bullough, R., Hartley, C. S., Hirth, J. P., Pergamon Press, Oxford, England

Argon, A. S., and Shi, L. T., 1982, Acta Metall. 31, 499

Argon, A. S., and Shi, L. T., 1983, in Amorphous Materials: Modeling of Structure and Properties, ed. Vitek, V., 279

Argon, A. S., 1996, in Physical Metallurgy, ed. Cahn, R. W., Haasen, P., North-Holland, Amsterdam

Argon, A. S., and Veprek, S., 2002, Mat. Res. Soc. Symp. Proc. Vol. 697, P1.2

Balamane, H., Halicioglu, T., Tiller, W. A., 1992, Phys. Rev. B46, 2250

Bazant, M. Z., Kaxiras, E., Justo, J. F., 1997, Phys. Rev. B56, 8542

Bertsekas, D. P., 1999, Nonlinear Programming, Athena Scientific, Belmont, MA

Brent, R. P., 1973, Algorithms for Minimization without Derivatives, Prentice-Hall, Englewood Cliffs, NJ

Broughton J. Q., Li, X. P., 1987, Phys. Rev. B35, 9120

Brown, D., Neyertz, S., 1995, Mol. Phys. 84, 577

Bulatov, V. V., Argon, A. S., 1994, Mod. Simul. Mater. Sc. 2, 167; 185; 203

Chaudhari, P., Levi, A., Steinhardt, P., 1979, Phys. Rev. Lett. 43, 1517

Cherns, D., Jenkins, M. L., White, S., 1980, in Electron Microscopy and Analysis 1979, Inst. Phys.: London

Cohen, M. H., and Turnbull, D., 1959, J. Chem. Phys. 31, 1164

Conrad, H., 1963, The Relation between the Structure and Mechanical Properties of Metals, Proceedings of the conference held at the National Physical Laboratory, Teddington, Middlesex on the 7th, 8th and 9th January, 1963, Her Majesty's Stationary Office, London.

Davidovic, M., Stojic, M., Jovic, Dj., 1983, J. Phys. C16, 2053

De Berg, M., Van Kreveld, M., Overmars, M., Schwarzkopf, O., 2000, Computational Geometry: Algorithms and Applications, Springer, Berlin

Deng, D., Argon, A. S., Yip, S., 1989, Phil. Trans. R. Soc. Lond. A329, 549; 575; 595; 613

Evans, D. J., and Morriss, G. P., 1983, Phys. Lett. 98A, 433

Evans, D. J., and Morriss, G. P., 1984, Comput. Phys. Rep. 1, 297

Eyring, H., 1936, J. Chem. Phys. 4, 283

Furukawa, K., Shimbo, M., Fukuda, K., Tanzawa, K., 1986, Extended Abstracts of the 18th (1986 International) Conference on Solid-State Devices and Materials, Tokyo, B-9-1 (pp.533-536)

Gilman, J. J., 1968, in Dislocation Dynamics, ed. A. R. Rosenfield *et al.*, McGraw-Hill, New York

Haile, J. M., 1997, Molecular Dynamics Simulation: Elementary Methods, John Wiley & Sons
Hall, E. O., 1951, Proc. Phys. Soc. London B64, 747
Hoover, W. G., 1983, A. Rev. Phys. Chem. 34, 103
Huang, K., 1987, Statistical Mechanics, John Wiley & Sons, New York
Hutnik, M., Gentile, F. T., Ludovice, P. J., Suter, U. W., Argon, A. S., 1991, Macomolecules 24, 5962; 5970
Justo, J. F., Bazant, M. Z., Kaxiras, E., Bulatov, V. V., Yip, S., 1998, Phys. Rev. B58, 2539
Kantor, Y., and Webman, I., 1984, Phys. Rev. Lett. 52, 1891
Kauzmann, W., 1948, Chem. Rev. 43, 219
Keblinski, P., Phillpot, S. R., Wolf, D., Gleiter, H., 1996a, Acta. Mater. 45, 987
Keblinski, P., Phillpot, S. R., Wolf, D., Gleiter, H., 1996b, Phys. Rev. Lett. 77, 2965
Keblinski, P., Bazant, M. Z., Dash, R. K., Treacy, M. M., 2002, Phys. Rev. B66, 064104
Kluge, M. D., and Ray, J. R., 1988, Phys. Rev. B37, 4132
Laaziri, K., Kycia, S., Roorda, S., Chicoine, M., Robertson, J. L., Wang, J., Moss, S. C., 1999, Phys. Rev. Lett. 82, 3460
Luedtke, W. D., Landman, U., 1989, Phys. Rev. B40, 1164
Lund, A. C., Schuh, C. A., 2003, Acta. Mater. 51, 5399
McClintock, F. A., and Argon, A. S., 1966, Mechanical Behavior of Materials, Addison-Wesley, Reading, MA
Mott, P. H., Argon, A. S., Suter, U. W., 1992, J. Comput. Phys. 101, 140
Mott, P. H., Argon, A. S., Suter, U. W., 1993, Phil. Mag. A 67, 931
Nakhmanson, S. M., Mousseau, N., 2002, J. Phys.-Condens. Mat. 14, 6627
Olmsted, D. L., Hardikar, K. Y., Phillips, R., 2001, Mod. Simul. Mater. Sc. 9, 215
Petch, N. J., 1953, J. Iron Steel Inst. 174, 25
Phillips, J. C., 1979, J. Non-cryst. Solids 34, 153
Phillips, J. C., 1981a, J. Non-cryst. Solids 43, 37
Phillips, J. C., 1981b, J. Non-cryst. Solids 44, 17
Phillpot, S. R., Yip, S., Wolf, D., 1989, Computers in Physics Nov-Dec, 20
Polak, E., and Ribiere, G., 1969, Rev. Fr. Inform. Rech. O. 3, 35
Ren, Q., Joos, B., Duesbery, M. S., 1995, Phys. Rev. B52, 13223
Rose, H., Smith, J. R., Ferrante, 1983, J., Phys. Rev. B28, 1835
Schiotz, J., Di Tolla, F. D., 1998, Jacobsen, K. W., Nature 391, 561
Schiotz, J., and Jacobsen, K. W., 2003, Science 301, 1357
Stillinger, F. H., Weber, T. A., 1983, Phys. Rev. A28, 2408
Stillinger, F. H., Weber, T. A., 1985, Phys. Rev. B31, 5262
Tanemura, M., Ogawa, T., Ogita, N., 1983, J. Comput. Phys. 51, 191
Tersoff, J., 1986, Phys. Rev. Lett. 56, 632
Theodorou, D. N., Suter, U. W., 1985, Macromolecules 18, 1467
Theodorou, D. N., Suter, U. W., 1986, Macromolecules 19, 379
Thorpe, M. F., Jacobs, D. J., Chubynsky, M. V., Phillips, J. C., 2000, J. Non-cryst. Solids 266-269, 857
Thompson, M. O., Galvin, G. J., Mayer, J. W., Peercy, P. S., Poate, J. M., Jacobson, D. C., Cullis, A. G., Chew, N. G., 1984, Phys. Rev. Lett. 52, 2360
Turnbull, D., Cohen, M. H., 1958, J. Chem. Phys. 29, 1049

Turnbull, D., Cohen, M. H., 1961, J. Chem. Phys. 34, 120
Van Vliet, K. J., Suresh, S., 2002, Phil. Mag. A82, 1993
Veprek, S., Argon, A. S., 2002, J. Vac. Sci. Technol. B20, 650
Wolf, D., Wang, J., Phillpot, S. R., Gleiter, H., 1995, Phys. Lett. A205, 274
Wooten, F., Winer, K., Weaire, D., 1985, Phys. Rev. Lett. 54, 1392
Yamakov, V., Wolf, D., Phillpot, S. R., Mukherjee, A. K., Gleiter, H., 2001, Acta. Mater. 49, 2713
Yamakov, V., Wolf, D., Phillpot, S. R., Mukherjee, A. K., Gleiter, H., 2002, Nature Materials 1, 1
Yip, S., 1998, Nature 391, 532
Zachariasen, W. H., 1932, J. Am. Chem. Soc. 54, 3841
Zallen, R., 1979, in Fluctuation Phenomena, ed. E. W. Montroll, North-Holland, New York
Ziman, J. M., 1995, Principles of the Theory of Solids, Cambridge University Press, Cambridge, England